Contract # 954617

Laboratory for Atmospheric and Space Physics

SOLAR MESOSPHERE EXPLORER

EXPERIMENT DESCRIPTION

University of Colorado at Boulder
Boulder, Colorado 80309

EXPERIMENT DESCRIPTION

SOLAR MESOSPHERE EXPLORER

LABORATORY FOR ATMOSPHERIC AND SPACE PHYSICS

UNIVERSITY OF COLORADO

EXPERIMENT DESCRIPTION

Table of Contents

EXPERIMENT DESCRIPION

List of Figures

List of Tables

1.0 OBJECTIVES AND SIGNIFICANT ASPECTS

The Solar Mesosphere Explorer (SME) satellite experiments will provide a comprehensive study of atmospheric ozone and the processes which form and destroy it. Five instruments to be carried on the spacecraft will measure the ozone density and altitude distribution, monitor the incoming solar radiation, and measure other atmospheric constituents which affect ozone.

Ozone is present in the earth's atmosphere as a consequence of the photodissociation of molecular oxygen by solar ultraviolet radiation. Oxygen atoms that result from the dissociation process react with oxygen molecules to form ozone. Solar radiation also acts to destroy ozone by photodissociation, particularly in the middle ultraviolet. Oxygen atoms also break down ozone into molecular oxygen. Other atmospheric constituents react with ozone, sometimes in cyclic reactions that consume ozone while they themselves are regenerated. Atomic hydrogen and the hydroxyl and hydroperoxyl radicals, which are the photodissociation products of water vapor, catalytically destroy ozone. Other atmospheric species that react catalytically to destroy ozone are nitric oxide and nitrogen dioxide.

Water vapor occurs naturally in the atmosphere, but its abundance may vary, and this variation will affect the density of ozone. Nitric oxide and nitrogen dioxide also occur naturally by the oxidation of nitrous oxide, solar

proton events, and ionospheric reactions, but they may be injected in the atmosphere artificially as well. Recently, other atmospheric constituents have been identified as catalytic destroyers of ozone. Halogens and oxides of halogens belong to this class, and their origins lie at least partly in human activities.

As a result of the many theoretical studies of ozone photochemistry that have been carried out since 1930, the following general statements may be made about the behavior of ozone in the earth's atmosphere. The vertical distribution of ozone between about 40 and 80 km is determined mainly by photochemical processes. However, transport processes are primarily responsible for the distribution of ozone below 30 km and above 80 km. Above 80 km transport controls atomic oxygen, atomic hydrogen, and, thereby, ozone. In the altitude range 40 to 80 km, the amount and distribution of ozone is determined by the intensity and spectral distribution of solar ultraviolet radiation, by the abundance and distribution of minor atmospheric constituents, and by the temperature structure of the atmosphere (see, for example, Park and London, 1974).

The first objective of the SME satellite experiments is to determine what changes occur in the ozone distribution as a result of changes in the incoming solar radiation. A second objective is to measure all changes in the ozone density distribution in the altitude range 30-80 km and to

determine the causes of these changes. This will include simultaneous measurements of temperature, pressure, water vapor, nitrogen dioxide, near infrared airglow, and solar flux. For instance, solar protons events have been found to perturb significantly the chemical composition of the stratosphere and mesosphere through the production of NO and OH. The rates of production of these constituents can be calculated from data from satellite proton detectors (Crutzen et al., 1975, Frederick, 1975).

The instruments on SME will be a solar ultraviolet spectrometer, an ozone ultraviolet spectrometer, an infrared radiometer, an infrared spectrometer, and a nitrogen dioxide spectrometer. A solar proton alarm mechanism will also be carried to measure integrated solar flux in the range 30-500 MeV. The solar UV instrument will continuously measure the flux of the solar radiation in the wavelength region which dissociates molecular oxygen, the region in which ozone is photodissociated, and the Lyman alpha line which is primarily responsible for the dissociation of water vapor. Four different limb scanning instruments will measure the altitude distribution of ozone from 30 km to 80 km. The ozone UV spectrometer will measure the combination of ozone absorption and Rayleigh scattering in the middle ultraviolet region. A near infrared spectrometer will measure the 1.27μ emission from excited molecular oxygen resulting from the photodissociation of ozone. This instrument will also

measure near infrared hydroxyl emissions. The infrared radiometer will measure the thermal emission from ozone in the 9.6μ band, and carbon dioxide emission in the 15μ band will be measured to determine the temperature structure of the atmosphere. The infrared radiometer will also measure water vapor in the 6.3μ band. The nitrogen dioxide spectrometer will measure the nitrogen dioxide distribution in the 20-40 km region.

This satellite complement will have the unique capability of simultaneously measuring solar parameters that may produce changes in the ozone and the ozone abundance itself. These experiments are designed to determine what solar-terrestrial correlation exists and the photochemical path that leads to changes in ozone density. Additionally, other changes in the ozone abundance will be identified and distinguished from those caused by the sun.

2.0 INVESTIGATIVE APPROACH

2.1 Concept

2.1.1 Ozone Photochemistry

The dominant photochemical processes between 30 and 80 km involve ozone. Ozone is produced by

$$O_2 + h\nu(\lambda < 2420\ A) \rightarrow O + O \qquad (1)$$

$$O + O_2 + M \rightarrow O_3 + M \qquad (2)$$

where M is a third body, mainly N_2 and O_2.

Ozone is destroyed by the following reactions:

$$O_3 + h\nu(2000\text{-}8000\ A) \rightarrow O + O_2 \qquad (3)$$

and

$$O_3 + O \rightarrow O_2 + O_2 \qquad (4)$$

Reactions (1)-(4) were proposed by Chapman in 1930 and were believed adequate until the 1960s. However, rocket and balloon measurements showed less ozone than predicted, necessitating modifications of the theory involving catalytic ozone-destroying reactions.

Reaction (4) may be catalyzed in the following manner:

$$O_3 + A \rightarrow O_2 + AO$$
$$AO + O \rightarrow O_2 + A$$
$$\overline{O_3 + O \rightarrow 2O_2} \qquad (5)$$

The compound A may be H, NO, or Cl. H is dominant between 45 and 90 km. In order to model the most important catalytic ozone-reducing reactions, compounds of oxygen, nitrogen, and hydrogen must be considered (e.g., Hunt, 1966; Crutzen, 1971; Thomas and Bowman, 1972; Nicolet, 1970; Strobel, 1972, Park and London, 1974). Liu and Donahue (1974) and Hunten and Strobel (1974) have modeled the escape of hydrogen from the earth. The source of hydrogen is water and methane originating at the surface of the earth. Figure 2.1 shows some experimental and theoretical ozone profiles. Figure 2.2 shows a simplified reaction scheme of the odd hydrogen compounds.

In the stratosphere ozone is destroyed by NO and NO_2 via a set of reactions (5) where A = NO. The complete nitrogen chemistry must, however, consider reactions involving N, N_2, NO, NO_2, HNO_2, HNO_3, N_2O_5, and N_2O (Crutzen, 1970 and 1971). The natural source of NO is provided by the oxidation of N_2O, which is produced by bacteria in the soil (Adel, 1951; Bates and Hays, 1967; Crutzen, 1976). A potentially important manmade source of NO in the stratosphere is provided by stratosphere-flying aircraft (Crutzen, 1971;

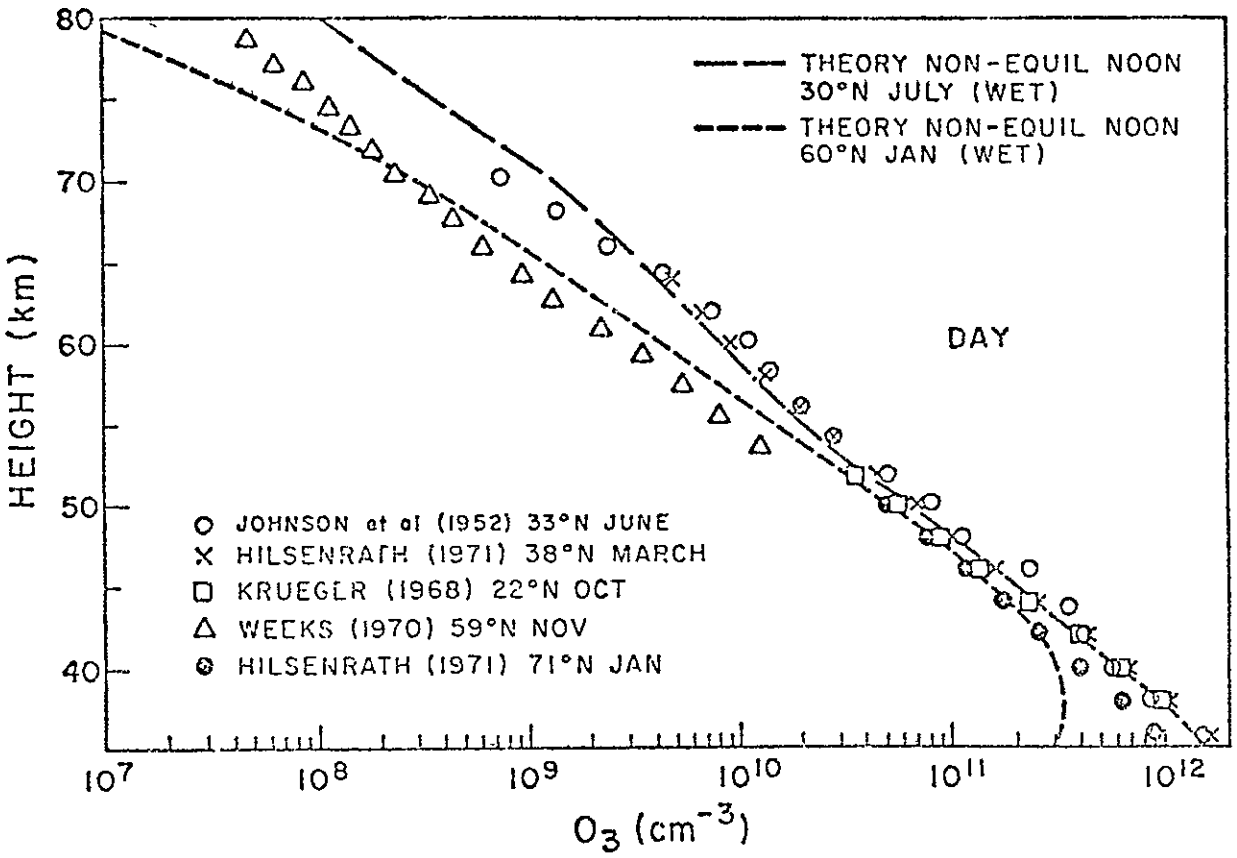

Figure 2.1 Ozone profiles show the density from 40 to 80 km. The measured and theoretical profiles vary by a factor of five. From Park and London (1974).

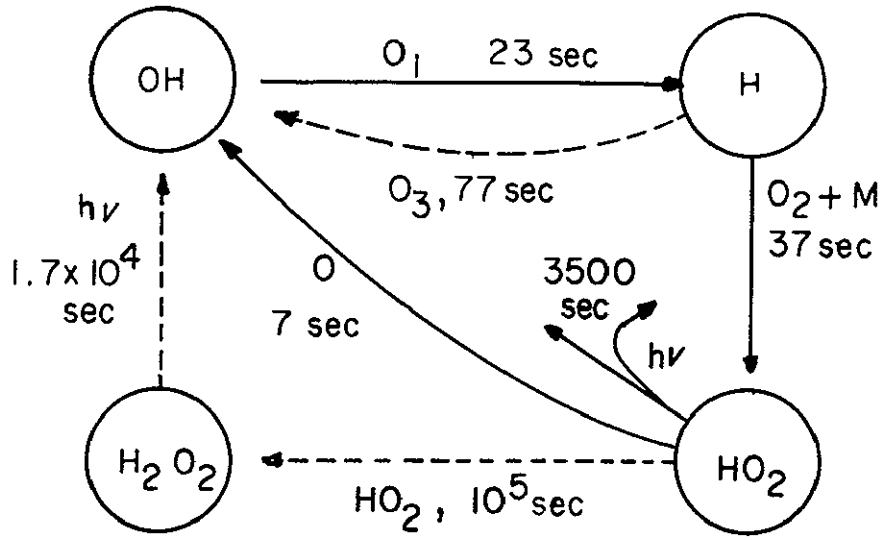

Figure 2.2 Simplified reaction scheme for odd hydrogen with time constants at 70 km. From Hunten and Strobel (1974).

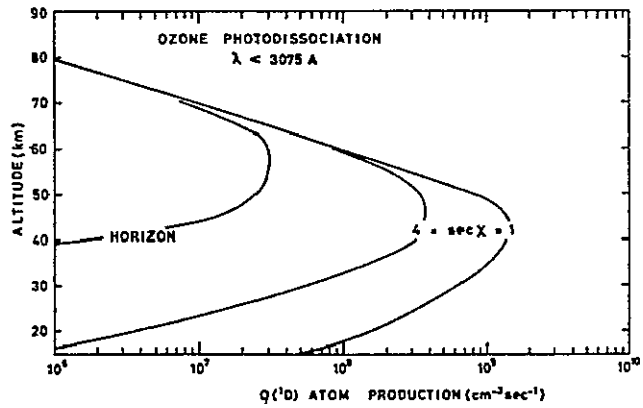

Figure 2.3 The altitude of ozone photodissociation for the sun on the horizon and overhead; sec χ = 1. From Nicolet (1970).

Johnston, 1971) and nuclear explosions (Johnston et al., 1973).

Very recently it has been pointed out that Cl may become the dominant catalyst for ozone destruction in the stratosphere (Molina and Rowland, 1974; Crutzen, 1974; Cicerone et al., 1974). The chlorofluorocarbons, F11 ($CFCl_3$) and F12 (CF_2Cl_2), used as aerosol propellents and refrigerants, are being released at an increasing rate at ground level. Inert below the tropopause, these gases are photodissociated in the stratosphere, thereby releasing Cl atoms. Effects of manmade threats to the ozone concentration are summarized in the 1975 Report of the Climatic Impact Committee of the National Academy of Sciences.

The driving energy for all photochemical processes is primarily provided by solar radiation. Most of the solar energy from 1600 A to 3100 A is absorbed in the mesosphere and stratosphere by O_2 and O_3. Dissociation of O_3 via reaction (3) occurs between 20 and 80 km as shown in Figure 2.3 for several sun angles. At wavelengths below 3100 A virtually all of the O_2 produced in reaction (3) is in the excited $O_2(^1\Delta_g)$ state which radiates at 1.27μ. Observation of this radiation in the mesosphere gives the altitude distribution of the O_3 destruction by solar photons. Radiation of shorter wavelengths 1750-2000 A is absorbed mostly by O_2 in the Schumann-Runge bands. The altitude of peak absorption varies between 60 and 90 km depending on the

absorption cross section and solar angle, Figure 2.4. The cross section for O_2 dissociation by Lyman α is small, and this radiation, therefore, penetrates the mesopause. Unit optical depth for Lyman α is near 75 km, and at this altitude changes in the Lyman α flux are preferentially felt by water vapor.

2.1.2 Measurement

The theoretical and measured ozone profiles are in only fair agreement in the mesosphere. The theoretical studies assume a standard temperature, solar flux, O_2 density, and other parameters which, of course, do not exactly apply to an actual ozone measurement. This limits the understanding of small effects which may be important. We propose to investigate more fully the ozone variations by simultaneous measurement of all relevant parameters. The ability of the ozone to react to a change in one of the photochemical inputs such as changes in solar radiation can be seen in Figure 2.5. For instance, at 70 km ozone and atomic oxygen will reach a new steady state in about three hours, a condition which chemical and air motion will not remove for about ten days. This means that if the solar spectrum changes so as to produce more ozone between 65 and 70 km it could be observed for several spacecraft orbits. Similarly, an injection of NO by solar proton events at lower levels (below 45 km) will lead to changes in ozone concentrations which can be studied in the stratosphere because of the very long photochemical lifetime of NO and NO_2.

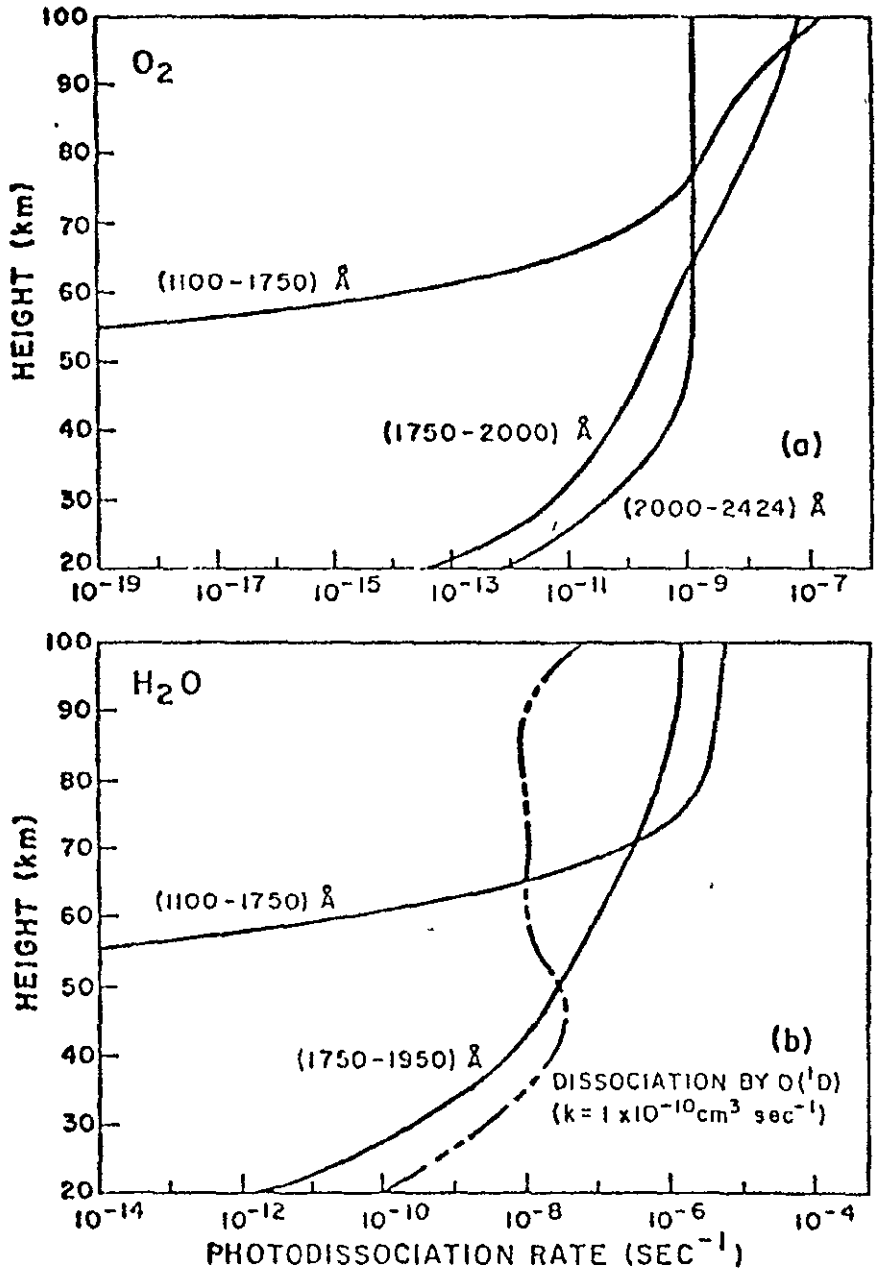

Figure 2.4 Photodissociation rates per molecule for oxygen and water. After the rate has decreased an order of magnitude, most of the energy has been deposited (i.e., in (a) the energy between 2000 and 2424 A is deposited between 24 and 40 km). From Park and London (1974).

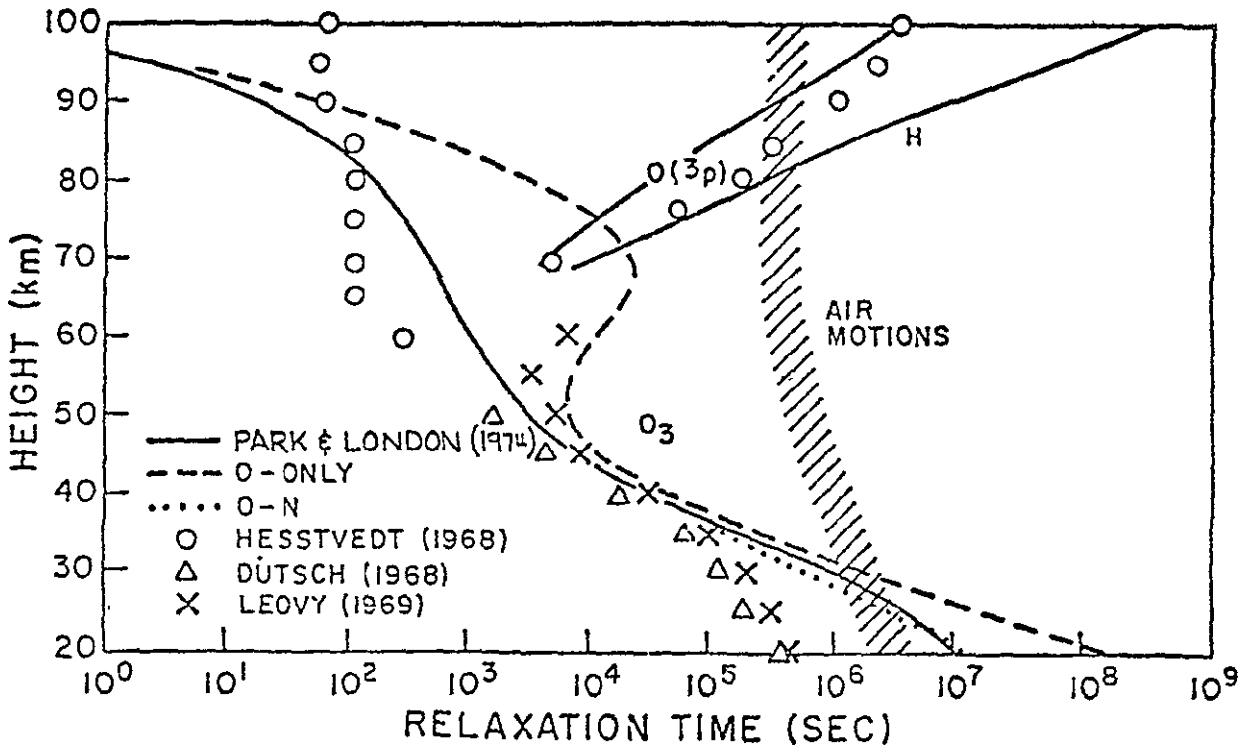

Figure 2.5 Relaxation times for ozone, atomic oxygen, and atomic hydrogen. From Park and London (1974).

To learn more about ozone photochemistry and the global-seasonal high altitude ozone variations, the following quantities need to be observed:

1. O_3 density
2. Solar flux (1600-3100 A and Lyman α)
3. Neutral temperature and density
4. H_2O density
5. 1.27μ airglow (O_3 photodissociation)

In addition, from proton flux and energy detectors on board this and other satellites, it will be possible to calculate the injection rate of NO and OH following solar proton events. Since three of the four measurements require the presence of sunlight, data will generally be taken during the day. The infrared instruments can measure O_3, H_2O, pressure, temperature, and airglow at night, and diurnal variations can, therefore, be inferred.

Each measurement to be made by the proposed satellite is discussed separately in the following sections.

2.1.3 Limb Scanning

All measurements except solar flux will be made by scanning through the limb. The limb scanning technique is used to obtain altitude information of optically observable phenomenon which occur below the satellite altitude. It has been used to obtain altitude and latitude profiles of the oxygen-green line emission from OGO-6 (Thomas and Donahue, 1972; Donahue et al., 1973), and it is currently being used

on AE-C and -D to obtain similar information on nitric oxide (Barth et al., 1973) and on Nimbus 6 for stratospheric temperature, pressure, and ozone (Gille and House, 1971)

The procedure for obtaining an altitude profile from a limb scan is described below for a simple case of an emitting species. As shown in Figure 2.6 light is emitted or scattered by molecules throughout a layer. The minimum altitude of the observation is h_o (as the satellite scans the limb, h_o changes). Assume that the number density of emitting species varies exponentially as many atmospheric parameters do, $n = n_1 e^{-h/H}$, where H is the local scale height. The intensity integrated along the slant path, l, is then

$$4\pi I_l(h_o) = g \int_{-\infty}^{\infty} n_1 e^{-h/H} \, dl$$

where g is the emission rate per atom or molecule. Using a good approximation of the Chapman function at 90° (Hunten, 1954), this expression is rewritten

$$4\pi I_l(h_o) = g n_1 \exp(-h_o/H) \sqrt{2\pi RH}$$

where R is the earth radius. The altitude variation of the emitting species is easily obtained from this expression. For a more complete variation of density of emitting species versus altitude, more complex mathematical methods must be

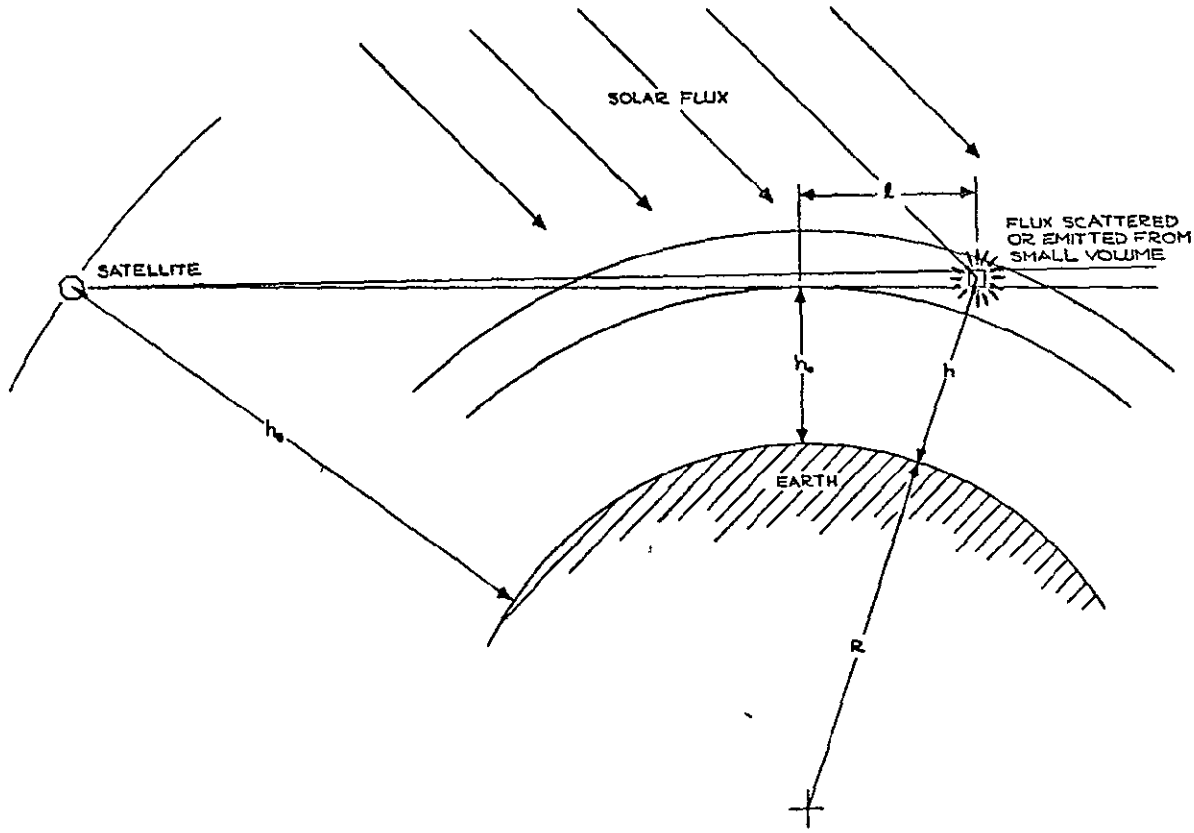

Figure 2.6 Illustration of limb scanning geometry (not to scale). Light emitted or scattered from each small volume along the line of sight is seen by the satellite instruments. Since the emission decreases exponentially, only a layer of a scale height thick needs to be considered.

used. It is interesting to compare limb scanning to vertical observations, for example, zenith observations from a rocket payload. It is easy to show that the vertical intensity is:

$$4\pi I_v(h_o) = g n_1 H \exp(-h_o/H).$$

The ratio of the two intensities is:

$$I_l/I_v = \sqrt{2\pi R/H} .$$

For a scale height, H, of 7 km, as is found in the mesosphere, the ratio is about 80, giving the limb scanning technique greater sensitivity than nadir-type observations. Another factor which may be handled in a similar fashion is absorption of photons along the slant path. Latitude variation is unfolded from limb scans obtained at successive positions in the satellite orbit.

Since the limb is viewed close to the bright disc, the instrument will be designed to reject off axis light. We have made a detailed analysis of this (Hord et al., 1970).

The altitude resolution will be 4 km, and one measurement will be obtained for each degree of latitude. The intrinsic latitude resolution of the limb scanning method has been discussed (Donahue et al., 1973).

2.1.4 O_3 Density

The O_3 density will be measured with the limb scanning UV instrument by observing the attenuation of Rayleigh scattered sunlight. Intensity measurements will be made at two wavelengths, one where the O_3 absorption is strong and one where it is weak. The ratio of the measured intensities, after normalization at high altitudes, yields the O_3 density. The absorption cross section is shown in Figure 2.7. As can be seen, the absorption decreases two orders of magnitude between 2550 A and 3100 A. As an example, for small O_3 densities the chosen wavelengths may be 2550 A and 2800 A. Referring to Figure 2.6, sunlight is Rayleigh scattered from molecules in each small volume but then must pass through a long column of atmosphere before reaching the satellite. The ozone cross section varies by a factor of 150 between 2550 A and 3100 A. The two wavelengths to be measured should be spaced approximately 250 A apart. With this spacing, the reference wavelength has a cross section a minimum of a factor of 3 less than the strong absorption wavelength, and both wavelengths are less than 3100 A. With a nominal rotation rate of 5 rpm, four pairs of wavelengths can be sampled before the satellite has travelled a distance comparable to the intrinsic latitude resolution of the limb scanning methods. This means that eight different wavelength measurements through the atmosphere can be combined to give the ozone concentration over

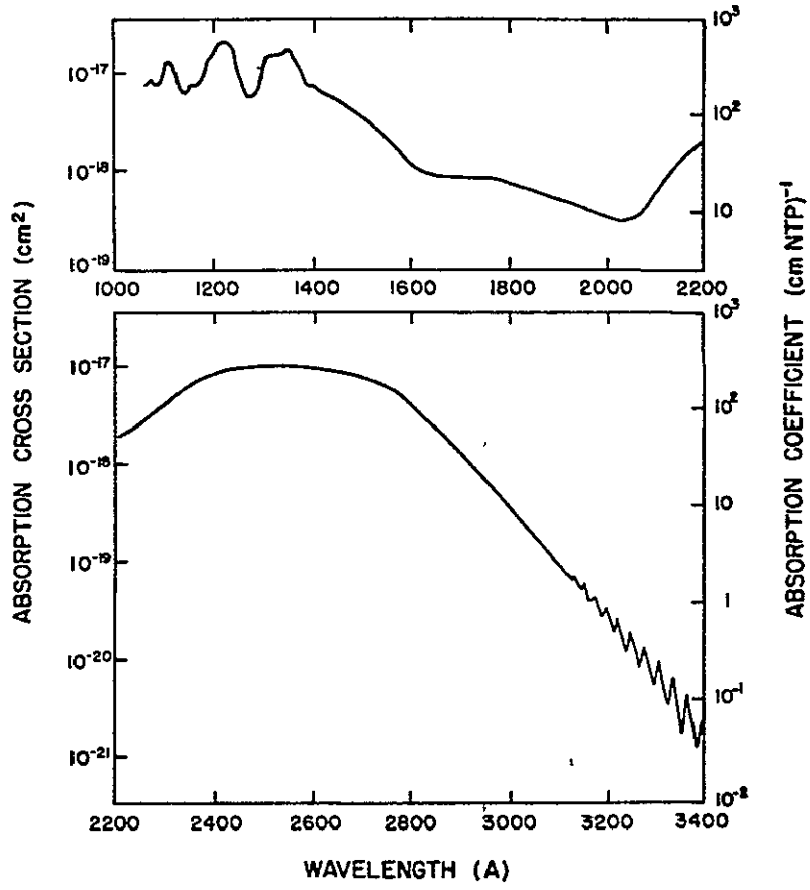

Figure 2.7 Absorption cross section of ozone. From Craig (1965).

the altitude range. The difference in absorption of the wavelength pairs along the column will allow the ozone concentration to be determined using radiative transfer theory.

Figure 2.8 shows a simulation of the intensity, I, (given in units of $4\pi I$ in kiloRayleighs/20 A) as a function of minimum ray height of observation. For this computation the ozone and Rayleigh scattering molecules in the model atmosphere have been assumed to have number densities and scale heights representative of this part of the atmosphere. Using an analysis similar to Hord et al. (1970) the governing equation for the intensity is

$$4\pi I = \pi F \; p(\Psi)\tau \; (2\pi R/H)^{\frac{1}{2}} \; T(\tau_o, H/H_o)$$

where πF is the solar flux, $p(\Psi)$ is the phase function of the scatterers, τ is the scattering optical thickness above the minimum ray height altitude, R is the distance of the minimum ray height point from the center of the earth, and H is the local scale height of the scattering atmosphere. Inversion of this equation leads to the ozone density. The function $T(\tau_o, H/H_o)$ takes into account the effect of ozone absorption, depending upon the amount and distribution above the minimum ray height. In the representation used here, T depends upon τ_o, the optical thickness of ozone above the minimum ray height point, and H/H_o, the ratio of the local

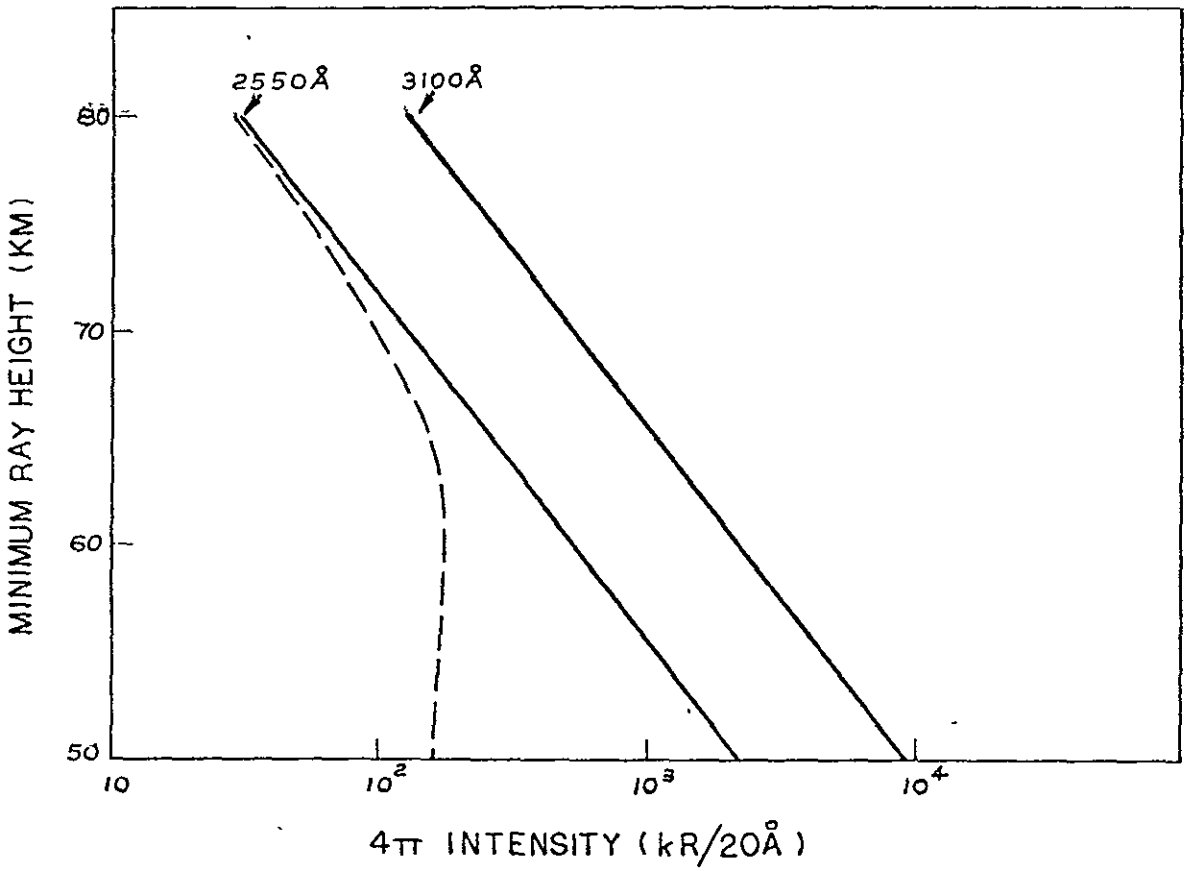

Figure 2.8 Ozone absorption of scattered sunlight. Solid lines show intensity of Rayleigh scattered sunlight. Strong ozone absorption at 2550 A causes a reduction of intensity (dashed line).

scale heights of the scattering and absorbing (ozone) atmospheres. As the amount of ozone, τ_o, becomes small, $T(\tau, H/H_o)$ approaches unity. In the absence of other scattering particles, the scattering optical thickness, τ, is the sum of the products of Rayleigh cross section and vertical column density of the molecular constituents. In this case, knowledge of the pressure at the sampling altitude (i.e., minimum ray height) is sufficient to specify τ.

In Figure 2.8, straight lines indicate the intensities expected at 2550 A and 3100 A, when T = 1, in the absence of ozone absorption. The curved line shows the effect of ozone absorption at 2550 A. Since the ozone cross section is 150 times less at 3100 A, the function, T, with ozone in the atmosphere is still very close to unity. The region of sensitivity for ozone measurements using 2550 A as the absorption wavelength is indicated in Figure 2.8. The minimum sample altitude that can be measured occurs when $\sqrt{(\pi R/2H_o)}\tau_o = 1$, and the maximum altitude is limited by sensitivity of the instrument to small changes in the intensity ratio. When the optical depth at 2550 A becomes large, the absorption wavelength can be shifted to a longer wavelength. In this manner we can probe to deeper layers of the atmosphere. A similar analysis using nadir observations has been employed by this laboratory (Anderson et al., 1969; London et al., 1972; London et al., 1976).

2.1.5 Solar Radiation

Changes in the solar radiation near 1800 A, for example, will affect the atomic oxygen formation, reaction (1), and hence the O_3 density. Such changes in the solar UV have been reported by Heath (1973). Changes lasting several hours should produce observable changes in O_3 concentration measured from one orbit to the next (more rapid fluctuations of solar input would be difficult to separate from latitude variations). In order to monitor the solar input to reaction (3), we will make measurements of the solar flux in the spectral region 2300 A to 2800 A. An increase in the solar Lyman alpha will produce an increase in odd hydrogen concentration resulting in a reduction of ozone and atomic oxygen. These wavelength intervals will normally be monitored several times per orbit; the sequence of observations may be varied in the light of experience gained during the mission. These data will be obtained using the 1/8 m spectrometer described in Section 3.4.

2.1.6 IR Radiation

Infrared radiation will be measured at four wavelengths with a height resolution at the limb of about 4 km. Two detector-filter combinations will be used to measure the thermal emission by H_2O at 6.3μ and O_3 at 9.6μ along limb paths. Using temperature and pressure information from the CO_2 bands at 15μ discussed below, these data will be inverted to obtain altitude-mixing ratio profiles for both

species. The results of the O_3 measurements will be compared to the O_3 densities obtained by the UV ozone experiment. A signal-to-noise ratio of one will be reached between 70 and 75 km, and the profiles can be extended to below 20 km. Such low-altitude densities will provide information on the variability of ozone in the lower stratosphere and will allow a cross calibration with various ground and balloon observations of the ozone concentrations at these levels.

The H_2O data will be obtained with a signal-to-noise ratio greater than one up to an altitude region between 67 and 74 km. The derived H_2O densities will provide information on the amount of odd hydrogen and hence the O_3 destruction rate by reaction (5) where H is the catalytic atom.

Two detector-filter combinations will have bandpasses centered on the 15μ CO_2 band. One has a wide bandpass ($\sim$3μ) and the other a moderately narrow bandpass ($\sim$1.7μ). Gille and House (1971) have developed an inversion technique which uniquely determines both pressure and temperature when instrument pointing is not precisely known. From the limb radiance profile for one of the channels, it is possible to determine the temperature profiles as a function of height relative to an assumed reference pressure level by an iterative technique. If the assumed reference pressure is incorrect, systematic errors in the inferred temperature

profile will occur. If a range of values for reference pressure is considered, a family of pressure-temperature curves will result, intersecting each other at an altitude near unit optical depth. A similar analysis of the other CO_2 channel will likewise result in a family of pressure-temperature curves intersecting at a different altitude due to the different opacities of the two channels. There is a single temperature-pressure curve, however, that is a member of both families. The two CO_2 channels have signal-to-noise ratios greater than one to above 85 km.

An analysis of the capabilities of the infrared experiment was carried out for the anticipated SME orbit and instrument parameters. A summary of the expected instrument performance is given in the instrument design section 3.2.5. The inversion technique employed was briefly outlined above and is considered in detail by Gille and House (1971).

Outgoing radiances were calculated using climatological temperature and mixing ratio profiles and then perturbed by the various types of anticipated errors. These include a smearing by the finite field of view, random radiance errors (noise equivalent radiance, NEN) and systematic (scale and bias) errors. These perturbed radiances were then inverted to give temperature, pressure, and mixing ratios and were compared with the original profiles.

Sample temperature inversions are shown in Figures 2.9a and 2.9b. The solid lines represent the inversion solution, and the dashed lines, the temperature profiles from which the original radiances were calculated. Good agreement is found throughout the region of experimental interest (50-80 km) even in the cold mesopause situation (Figure 2.9b) where signal-to-noise ratios are poorest. These results are for single limb scan situations. Since the instrument will be scanning roughly in the orbit plane and the horizontal extent of the tangent shell is of the order of 250 km, several scans can be merged together to reduce the random error component or the effective noise equivalent radiance. The effect of lower random errors on the temperature accuracy is summarized in Figure 2.10a for the entire profile (20-85 km), a layer in the lower experimental region (50-70 km), and a layer in the upper experimental region (70-85 km). The residual temperature error for zero random error reflects the degradation in the solution arising from the instrument field of view and the representation of the atmosphere in terms of a finite number of shells.

In addition, the unique pressure solution will give an accurate reference useful for all other experiments. The expected reference pressure accuracy is given in Table 2.1. Overall accuracy of the pressure or density profile will

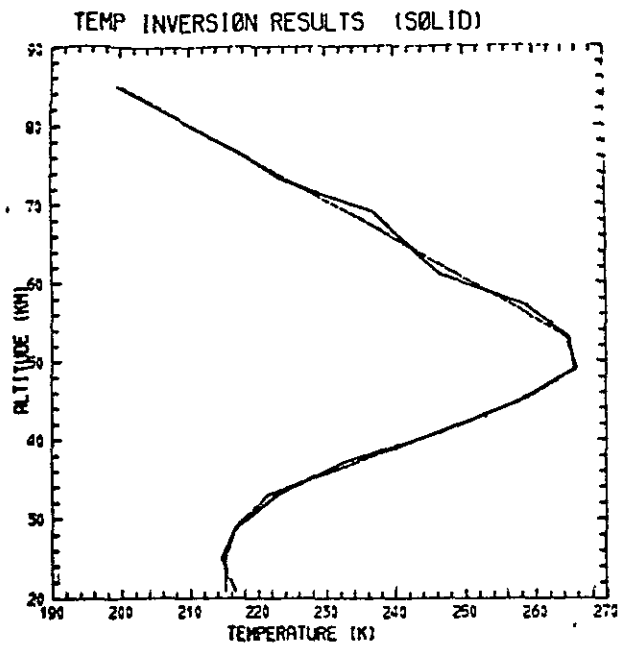

(a)

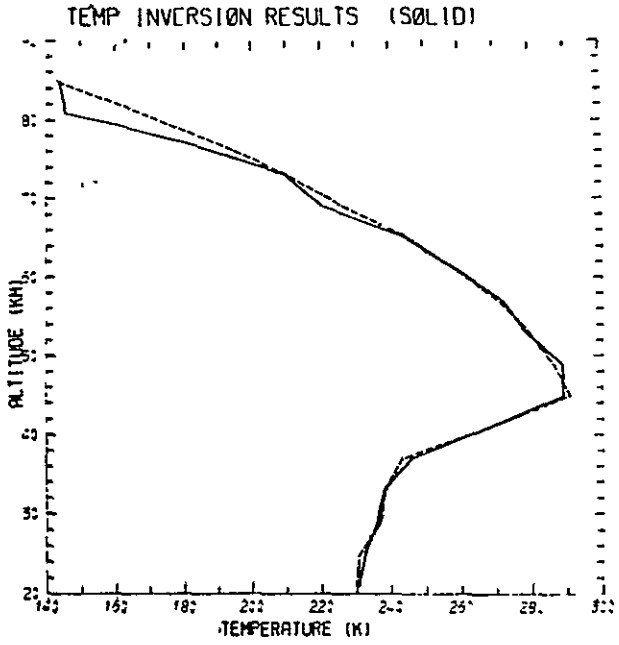

(b)

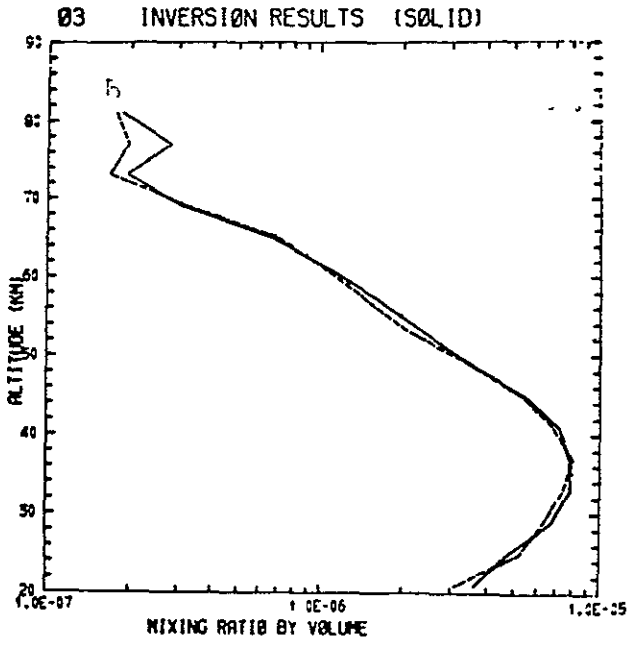

(c)

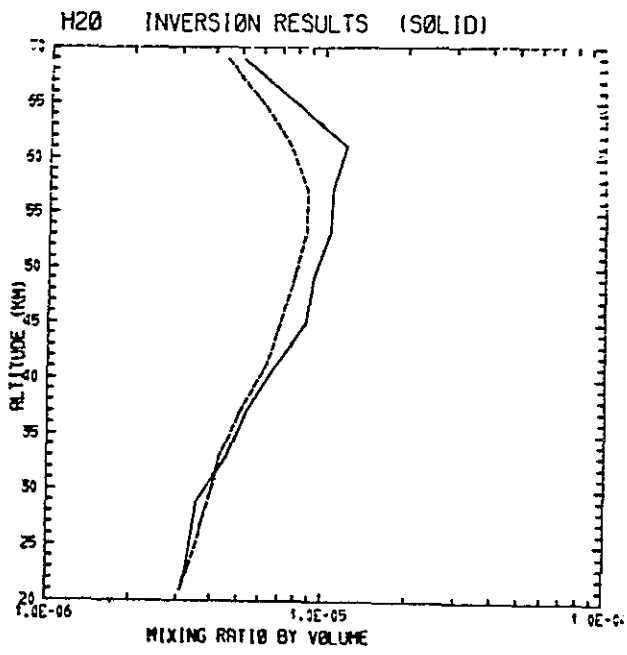

(d)

Figure 2.9 Sample inversions. (a) a temperature inversion for mid-latitude winter conditions. (b) for a cold mesopause. (c) and (d) show results for ozone and water in mid-latitude conditions. Dashed line is the assumed profile. Solid line is the inverted results when detector noise and scale and bias errors are added and then inverted.

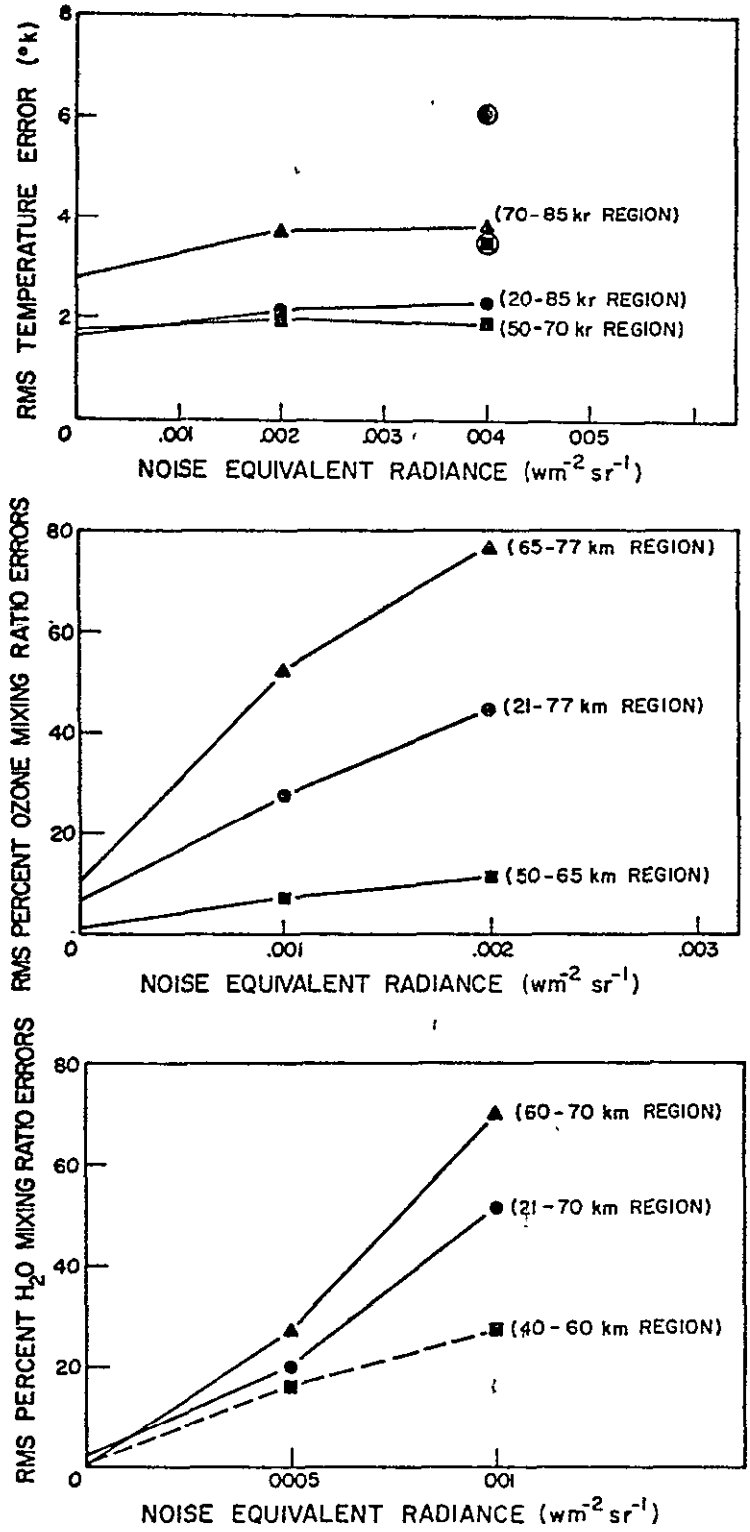

Figure 2.10 Expected error levels. The error increases as NEN increases for ozone and water. Even for perfect detectors, errors result from scale errors, bias errors, and the finite size of the field of view. These control the temperature errors except for very cold mesopause conditions (circled points). Since the radiance decreases with altitude, the errors increase.

depend on the accuracy of the reference pressure determination and to some extent on the accuracy of the temperature solution and any approximations made in the synthesis of the profiles. Systematic errors appear to be small. Relative errors are on the order of 1% or one tenth of the natural variability at the altitude selected.

REFERENCE PRESSURE ACCURACY
30 km Tangent Altitude
(Mean ± Std. Dev.)

True (mb)	Retrieved (mb)	True-Retrieved (mb)
9.878 ± 1.88	9.948 ± 1.15	-0.069 ± 0.125

TABLE 2.1

An ozone inversion is shown in Figure 2.9c. Good results with this technique can be obtained to about 70 km in most situations. The expected accuracies for mixing ratio determination are summarized in Figure 2.10b as a function of the random radiance error. Data obtained below 50 km will provide information on horizontal and vertical transports and the depth to which solar induced changes penetrate.

Results for an H_2O inversion in a moist upper stratosphere are shown in Figure 2.9d. Useful results can be obtained to about 65 km in most single scan cases. A

summary of expected accuracy versus random radiance error is shown in Figure 2.10c. When several scans of data are merged, mixing ratios can be inferred almost to the top of the region of interest.

2.1.7 1.27μ Airglow from $O_2(^1\Delta_g)$

Below 3300 A reaction (3) produces electronically excited $O_2(^1\Delta_g)$, which radiates at 1.27μ. This airglow has been measured by rockets (Evans and Llewellyn, 1970; Wallace and Hunten, 1968). Although there is some question as to the excitation of the $O_2(^1\Delta_g)$ in the nightglow near 90 km, there is no doubt that the dayglow is produced by reaction (3). Quenching of $O_2(^1\Delta_g)$ takes place by collisions with O_2 and N_2; quenching by O_3 can be neglected above 35 km (Evans and Llewellyn, 1970). The peak of the 1.27μ dayglow is near 50 km, making limb scanning in the 50 to 80 km region attractive.

In addition to measuring the 1.27μ emission, the airglow spectrometer will also scan between 0.8 and 2.4μ to observe the hydroxyl emission. These emissions are primarily produced by reactions involving odd hydrogen and include:

$$H + O_3 \rightarrow OH(v\leq 9) + O_2 \qquad (6)$$

$$O_2^{\ddagger} + H \rightarrow OH^{\ddagger} + O \qquad (7)$$

$$HO_2 + O \rightarrow OH^{\ddagger} + O_2 \qquad (8)$$

Each state may be excited directly or by cascade from above. Excitation by thermal process, solar resonance scattering, and hot atom collisions may also be important. Observations of these processes can be combined with our other data to identify the excitation mechanisms and to follow changes in high altitude odd hydrogen and atomic oxygen concentrations. Using twilight rocket measurements of $O_2(^1\Delta_g)$ and OH emission, Evans and Llewellyn (1973) have inferred ozone, atomic hydrogen, and atomic oxygen concentrations from 60 to 100 km.

2.1.8 Nitrogen Dioxide Experiment

The distribution of nitrogen dioxide in the 20-40 km region can be determined by inversion of limb scan profiles in a manner quite analogous to that employed in the ultraviolet ozone experiment. Use is made of the structured NO_2 absorption near 4500 A; from the present knowledge of the nitrogen dioxide abundance one may expect absorption at the limb to lie in the range 0.5 to 5% (Noxon, 1975). The mean vertical half width of the NO_2 distribution in the stratosphere is about 10 km and a vertical resolution of 3.5 km will define the shape. The instrument to be employed is another 1/8 m Ebert spectrometer with a telescope whose field is identical to the ultraviolet ozone experiment. The NO_2 observations will differ from the ozone observation in that the total NO_2 absorption seen at the limb will almost

never exceed 15% and the difference in absorption between two selected wavelength of high and low absorption (i.e., 4390 A and 4480 A) will not exceed 7%. This absorption corresponds to a vertical column of 10^{16} NO_2 molecules cm^{-2} distributed in altitude with a half thickness of 10 km, about the largest seen to date. In the event of an enhancement resulting from a solar proton event the limb absorption will naturally become larger and, possibly, the NO_2 absorption will become optically thick, requiring more detailed analysis.

Numerous aircraft measurements of NO_2 have never revealed less than $5 \times 10^{14}/cm^2$ vertical column corresponding to a maximum limb differential absorption of 0.4% which will be detectable. Low NO_2 abundances are regularly encountered north of 50° latitude in the winter; there is an abrupt decline of a factor of four in less than 5° of latitude. One object of the SME investigation will be to study the relationship between this NO_2 "ledge" and the ozone abundance. We will also search for a similar behavior in the southern hemisphere. At present there seems to be a strong possibility that the ledge is associated with the equatorial edge of the so-called winter circumpolar circulation vortex, seen at this altitude. The relationship of the high latitude NO_2 abundance to stratospheric warmings will be of considerable interest in view of the associated effects upon ozone.

2.1.9 Solar Proton Alarm

It is important to consider the effect of solar proton events on the temporal and spatial distribution of ozone in the stratosphere and mesosphere. Solar protons with energy between 30 and 500 MeV destroy water vapor in the mesosphere (Frederick, 1975) and produce NO in the stratosphere (Crutzen et al., 1975). Both result in a decrease in the ozone concentration in their respective regions. We will incorporate an instrument capable of detecting solar protons. This instrument subsystem will measure the integrated proton flux between 30 MeV and 500 MeV. Flux levels exceeding a threshold level will trigger an event pulse which will signal an opportunity to alter commands to the science instruments and experiment sequence. For example, if the SME is conducting experiments in the equatorial region, the solar proton event pulse could be used to change to an experiment sequence at high geomagnetic latitudes.

The solar proton alarm consists of a small (<1 cm^2), silicon, surface barrier detector. The output pulses will be integrated, and, if the flux exceeds a programmable threshold, an event pulse will be issued. The science instrument system may then either respond to the event pulse by changing the experiment sequence or ignoring it to continue the ongoing experiment.

The detector will be mounted in the skin of the satellite and will be omnidirectional due to the satellite rota-

tion. The detector can be miniaturized with simplified electronic design since it measures only the total flux and not the energy spectra of the incoming particles. Details of the particle spectra will be available from more sophisticated instruments aboard other satellites, for example, SMS/GOES or one of the advanced TIROS satellites.

2.2 Methods and Procedures

The instruments will scan the limb by looking radially from a slowly rotating satellite (about 5 revolutions per minute). The different instruments will be boresighted to scan the horizon simultaneously. To increase the ease of data reduction, and to make the measurements more meaningful, the limb scan will be in the orbit plane. See Figure 2.11.

The instruments will be programmed to take only data pertinent to the investigation. Each instrument will look radially from the spinning satellite (5 rpm) and will take data only while looking at the limb. This will reduce the data rate by a factor of 100. The simplest data taking procedure allows each instrument to take 20 samples as its field of view crosses the limb on each spacecraft rotation. Unless we are in a real time data mode, such a procedure will quickly fill the on board memory. Therefore, since fine latitude coverage ($<1°$) is not always necessary, measurements which are not required to be simultaneous will be independently programmed for fine to coarse coverage by

sampling every nth revolution of the satellite. By this method we will select the proper balance of data. For example, we may sample the UV O_3 detector each revolution to obtain fine coverage (1° of latitude), the IR temperature every fourth revolution (4° of latitude), and the IR O_3 and 1.27μ every sixteenth revolution for cross reference only. During the reference orbits, the solar spectrometer will monitor several preselected wavelengths instead of the entire solar spectrum.

The data will be reduced using a minicomputer system similar to ones used at this laboratory for Mariner 9. Each day the recorded raw data will be reduced from limb profiles to altitude profiles. At any time an experiment change in instrument timing, duty cycle, or wavelength is required, the necessary commands would be programmed and sent to the satellite. Further data reduction would be tied to photochemical models, altitude cross sections, global and seasonal maps.

2.3 Preflight Studies

The preflight studies will include development of data reduction programs and a photochemical model. The data reduction programs will invert the limb profiles producing altitude profiles. These inversion programs will be developed at several levels of sophistication for each instrument. These programs will be tested to determine the limits

of satisfactory operation. The entire process will be checked with expected data for different circumstances.

The photochemical models will be similar to those now being used by London and Crutzen (for example, Park and London, 1974; Crutzen, 1975; Crutzen and Isaksen, 1975). The models will use the altitude profiles for each instrument and will isolate those variations in ozone concentration caused by changes in the solar flux from the total variations.

Efficient output storage will facilitate production of global maps, seasonal maps, and solar correlations, all directed toward a more sophisticated understanding of the photochemistry of the mesosphere. With these programs tested and working prior to launch, operation and data reduction will be smooth and efficient soon after launch. A study of other possible experiments which could be performed for short periods with these versatile instruments will be undertaken.

2.4 Orbit and Mission Lifetime

The desired orbit is a constant local time orbit at 3 pm - 3 am. This will be a polar orbit and, hence, will give complete latitude coverage. The constant local time orbit allows investigation of seasonal effects and removes the diurnal effect from investigations of latitude, longitude, seasonal, and solar variation. The ideal orbit

should be circular, giving a uniform viewing geometry, and should be chosen to be as low as possible for optimum altitude resolution but sufficiently high to last one year, about 400 km. The orbit and satellite orientation is shown in Figure 2.11.

2.5 Review of Investigative Approach

Ozone is subject to many influences throughout the atmosphere. In recent years our understanding of the photochemistry of ozone in the presence of minor constituents such as "odd hydrogen," "NO_x," and "ClO_x" has greatly increased, to the point where extensive measurements are needed to verify and extend this understanding. SME is intended to investigate the relationship between ozone, solar flux, water vapor, and temperature in that region of the atmosphere (mesosphere) where other influences are less important and to establish in what areas these relationships break down as other influences begin to dominate. The photochemical and transport processes are summarized in Figure 2.12.

2.5.1 Ozone-Water Photochemistry

In the lower and middle mesosphere, the destruction of ozone is catalyzed by the "odd hydrogen" (H, OH, HO_2) produced by solar photodissociation of water vapor. The most important reactions in the catalytic cycles are:

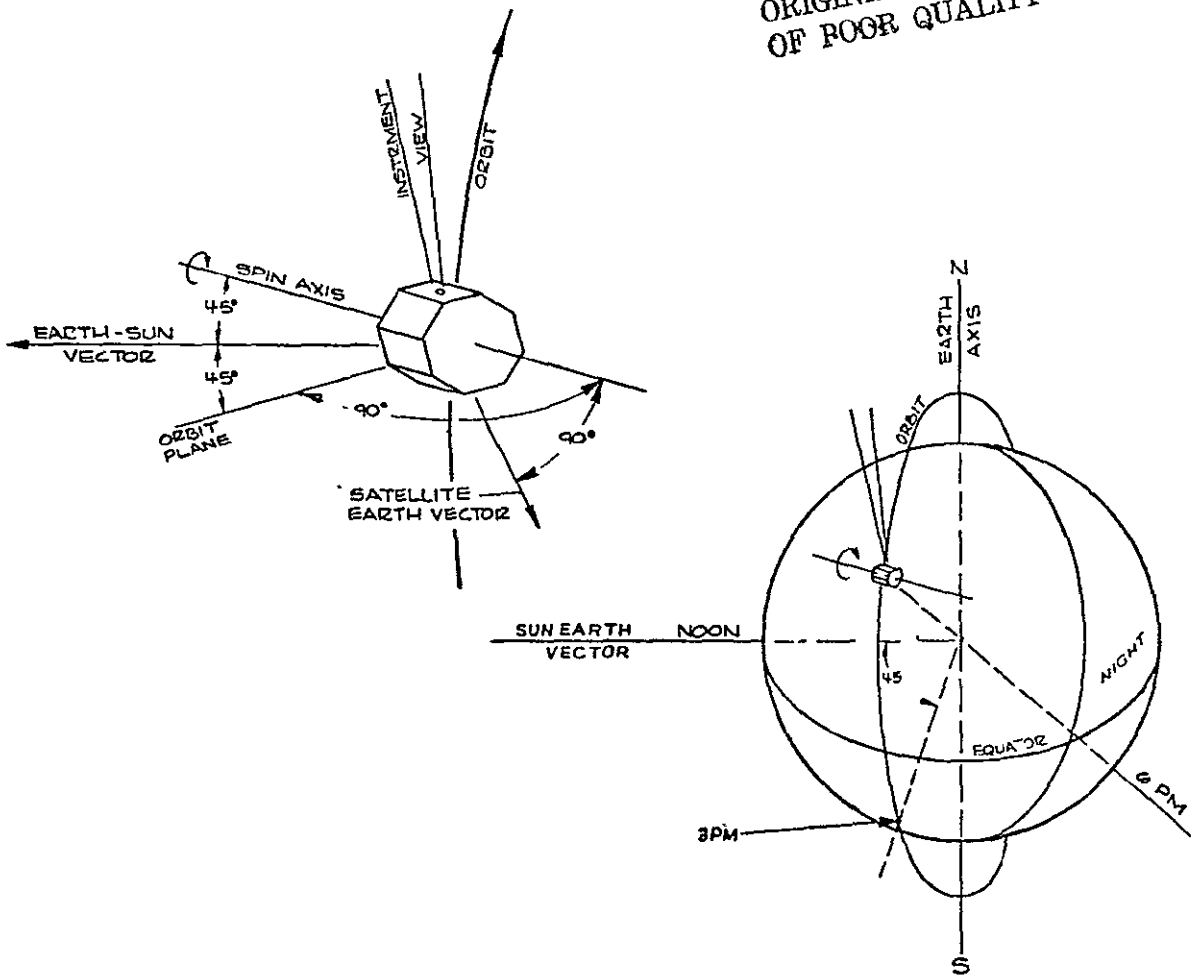

Figure 2.11 Satellite orbit. The orbit is a 3 a.m.-3 p.m. constant local time orbit. The satellite is oriented with spin axis normal to the orbital plane and perpendicular to the satellite/earth vector. The instruments look radially and, hence, scan the limb in the orbital plane.

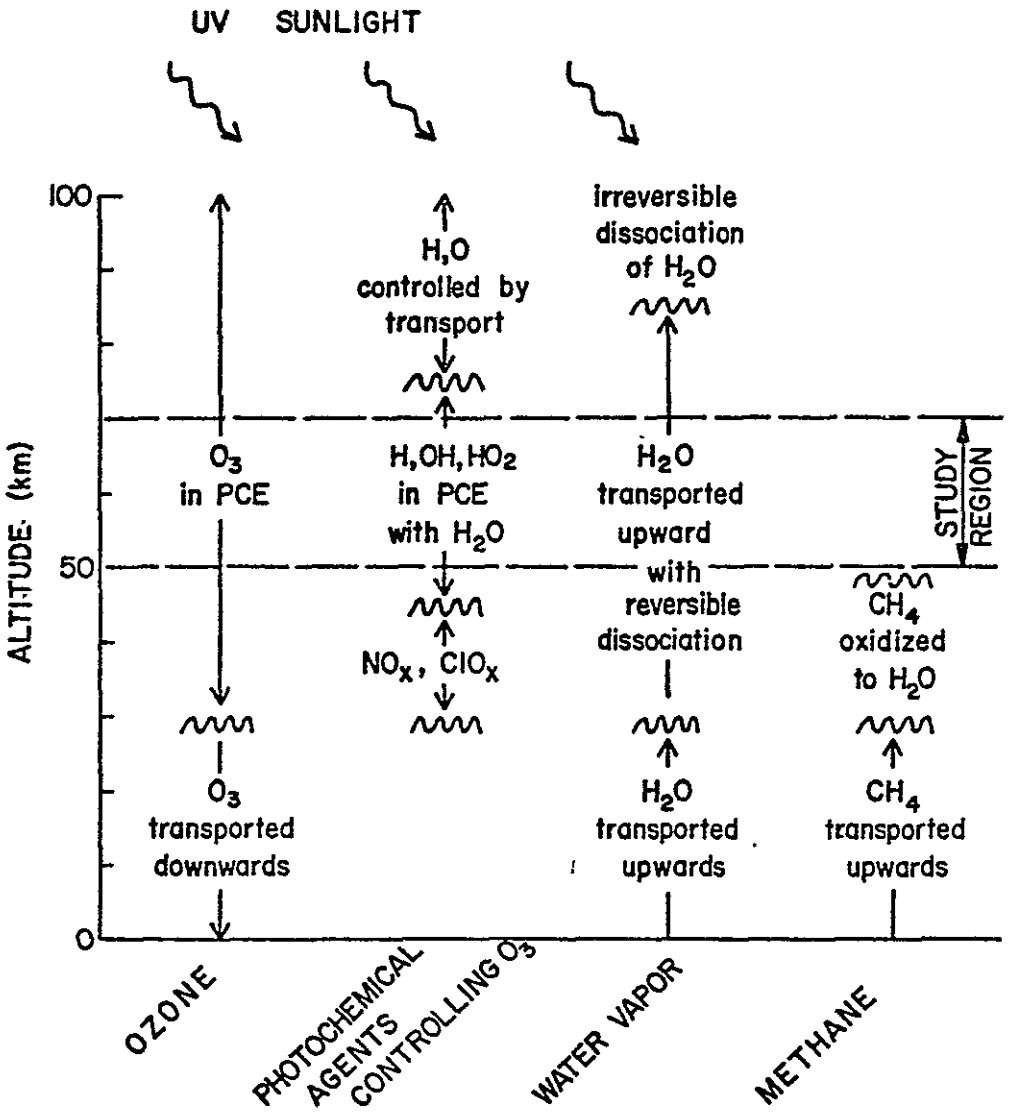

Figure 2.12 Summary of the major influences on ozone in different atmospheric regions.

$$H + O_2 + M \rightarrow HO_2 + M \quad (9)$$

$$HO_2 + O \rightarrow OH + O_2 \quad (10)$$

$$H + O_3 \rightarrow OH + O_2 \quad (11)$$

$$OH + O \rightarrow H + O_2 \quad (12)$$

and the processes controlling the abundance of odd hydrogen are:

$$H_2O + h\nu \rightarrow H + OH \quad (13)$$

$$OH + HO_2 \rightarrow H_2O + O_2 \quad (14)$$

$$O(^1D) + H_2O \rightarrow 2OH \quad (15)$$

Below 80 km, odd hydrogen is in photochemical equilibrium with water vapor, which is reformed as fast as it is dissociated. Above 80 km the destruction of water vapor rapidly becomes irreversible, largely because the three-body reaction converting H to HO_2 becomes slow. The hydrogen escapes upwards by eddy diffusion, the HO_2 (and consequently OH) density drops rapidly, and water is no longer re-formed. Thus, throughout much of the mesosphere, the distribution of H_2O is determined by an upward flow to the sink above 80 km.

Under these conditions the photochemical scheme is completely determined by measurements of O_3, H_2O, solar flux which dissociates O_2, H_2O, and O_3, and the temperature (which affects several important reaction rates). Accurate reactions rates are, of course, essential to the interpretation of the measurements. Manipulation of the continuity

equations for the various components of the scheme (Nicolet, 1974) shows, for example, that O_3 is proportional to the ratio of the photodissociation coefficients of O_2 and O_3 (determined by the solar flux) and inversely proportional to the square root of the photodissociation rate of water vapor (determined by the solar flux and the H_2O abundance). In contrast, in the absence of water vapor ozone destruction proceeds by:

$$O + O_3 \rightarrow 2O_2, \qquad (4)$$

and it is easily shown that O_3 varies as the square root of the ratio of photodissociation coefficients of O_2 and O_3.

SME will measure the quantities controlling the O_3-H_2O photochemistry. In the mesosphere O_3 is strongly photodissociated between 2100 and 3100 A, while O_2 is dissociated in the Schumann-Runge bands and Herzberg continuum (1750-2424 A). H_2O is dissociated shortward of 2400 A (again in the mesosphere) but more importantly by Lyman alpha (1216 A).

Molecular hydrogen and methane are also potential sources of odd hydrogen in the mesosphere. H_2 becomes the dominant hydrogen-bearing constitutent near 80 km; however, it is destroyed only slowly by the reaction:

$$O(^1D) + H_2 \rightarrow OH + H \qquad (16)$$

and its contribution to odd hydrogen production never exceeds 10% of the H_2O source. Methane contains about 10% of

the available hydrogen at the stratopause but, unlike water vapor, its destruction in the mesosphere is irreversible, and its mixing ratio should decline rapidly with altitude. Thus, neither H_2 nor CH_4 is a significant source of odd hydrogen in the mesosphere.

2.5.2 Limits of the O_3-H_2O Photochemical Model

The O_3-H_2O model breaks down near the mesopause because of the loss of H by diffusion and below about 40 km because of the increasing importance of NO_x and ClO_x. SME will detect the departures of the measurements from the O_3-H_2O model and will, therefore, demonstrate and measure the importance of these perturbing influences. Below 40 km the production of odd hydrogen by photodissociation of the H_2O drops off due to the increasing opacity of the atmosphere, and other catalysts become important. NO_x destroys O_3 via the reactions:

$$NO + O_3 \rightarrow NO_2 + O_2 \qquad (17)$$

$$NO_2 + O \rightarrow NO + O_2. \qquad (18)$$

The abundance of NO_x depends on the upward flow of N_2O into the stratosphere where it is attacked by $O(^1D)$,

$$N_2O + O(^1D) \rightarrow 2NO, \qquad (19)$$

and/or the destruction of NO_2 by

$$NO_2 + OH + M \rightarrow HNO_3 + M \qquad (20)$$

in the same altitude region. NO is the dominant form of NO_x above 40 km. The response of NO to changes in the ambient atmosphere and solar flux is very complex, and SME will help our understanding of this response through the detection of departures of ozone from its O_3-H_2O model values.

An increasingly important destruction mechanism for ozone below 40 km is the chlorine cycle·

$$Cl + O_3 \rightarrow ClO + O_2 \qquad (21)$$

$$ClO + O \rightarrow Cl + O_2. \qquad (22)$$

One source of free chlorine is the photodissociation of chlorofluorocarbons whose abundance is steadily increasing. At present levels this process does not compete with the NO_x cycles in the upper stratosphere.

2.5.3 Atmospheric Transport

The time scale for vertical transport in the 50-70 km region lies in the range 10-100 days. A more precise statement is not possible, in part because there is little observation or theory to indicate the magnitude and nature of vertical mixing processes in this region. Furthermore, mixing is likely to be sporadic, that is, much more rapid at some times than at others. We can safely assert that

species involving chemical reactions requiring a few days or less will be in equilibrium with each other, and, conversely, species reacting only on time scales of a year or more will have their distribution largely controlled by transport. In the region under consideration, the odd oxygen species depend on fast reactions and so are all in chemical equilibrium. However, the species CH_4, H_2, and H_2O are destroyed (or generated) more slowly, and the possible role of transport in determining their distribution must be established. Methane has a chemical lifetime on the order of 100 days at 50 km so its distribution above is likely to be strongly influenced by transport. However, its concentration is relatively insignificant compared to water vapor at these levels. Because of the absence of sources above the earth's surface and slow transport in the lower stratosphere, mixing ratios of CH_4 decrease slowly above the tropopause from values greater than 1 ppm. Observations have shown it to be 0.25 ppm at 50 km, and at higher altitudes it should be less (compared with 3 ppm water vapor) (Ehhalt et al., 1973). Molecular hydrogen evidently has photochemical time scales shorter than 10 days above 50 km, and the model of Hunten and Strobel (1974) indicates its abundance to be two orders of magnitude less than that of H_2O. Water vapor has dissociation time scales in the range 10-100 days from 50-70 km as indicated by Figure 2.4. Thus, its concentration in the mesosphere is probably not uniformly

mixed but controlled jointly by transport and chemistry. Changes in water vapor concentration as monitored by the experiment will indicate the action either of transport processes or of changing solar activity. Monitoring the temperature field may indicate possible unusual transport activity.

The loss of H by upward transport near the mesopause and eventual escape from the earth depends on the vigor of eddy mixing. This is known to be a variable quantity, both in time and location. The effect of upward transport of H is to reduce the odd hydrogen densities and slow the destruction of O_3; thus an increase in eddy mixing should lead to an increase in O_3. Because the vertical and horizontal mixing time scales are normally longer than several days, local effects may be observed on the satellite passes over a given location once per day. By the same token, however, transient local effects with time scales of a day or less are not observable.

2.5.4 Solar Radiation

The spectrum of the solar radiation that penetrates to the 50-70 km altitude region includes Lyman alaph, 1216 A; the long wavelength portion of the Schumann-Runge continuum, 1700-1750 A; the Schumann-Runge bands, 1750-2050 A; and the Herzberg continuum, 2050-2424 A (Figure 2.4). The wavelength interval between 1700 and 2424 A is chosen since solar ultraviolet radiation in this region determines the

rate of production of oxygen atoms in the 50-70 km region. At about 2085 A, the solar spectrum changes character. Longward of this wavelength the spectrum is primarily a continuum, shortward, the continuum intensity drops, and some emission lines appear. Since the wavelength region between 1700 and 2085 A is particularly suspect of being variable, this region will be monitored carefully. In the wavelength region 2000-3100 A ozone is photodissociated in the Hartley continuum. While this spectral region is less likely to be variable, it also will be monitored. The variation in solar Lyman alpha is on the order of $\pm$30% (Vidal-Madjar et al., 1973), and changes in the Lyman alpha flux is preferentially felt by atmospheric water vapor near the altitude of unit optical depth, between 70 km and 75 km. An increase in odd hydrogen concentration results in a reduction of ozone and atomic oxygen. For maximum solar flux conditions, the ozone concentration at 75 km is calculated to be near 80% of its value for minimum flux conditions (Frederick, 1975).

2.5.5 Summary of Observations

In the altitude region where photochemical equilibrium exists, 40-80 km, the time constant for changes in ozone density varies from 10^4 seconds to 10^5 seconds (Figure 2.5). Over this same altitude interval, the density of ozone decreases from several times 10^{11} molecules cm^{-3} to 10^8 molecules cm^{-3} (Figure 2.1). Within this altitude region,

the interval between 50 and 70 km is chosen to test the primary objective of the experiment, the response of ozone to changes in the solar ultraviolet flux. In this altitude range the time constants are sufficiently short for changes to be detected, and the ozone densities are sufficiently large to lie within the detection limits of the instruments Measurements of the other parameters relevant to the ozone-water photochemistry will also be made for the 50-70 km region. Figure 2.13 summarizes the altitude regions of interest and shows the measurement range of each instrument. In addition, incoming solar radiation which influences the ozone photochemistry will be monitored.

Ozone will be measured using the limb scanning ultraviolet spectrometer. Two wavelength regions will be measured simultaneously, one where ozone absorption occurs, the other where there is no absorption. The measurements may be made in the entire altitude range 40-70 km.

A limb scanning photometer that measures emission in the 1.27μ band of molecular oxygen will also measure ozone. Oxygen molecules in the excited $^1\Delta_g$ state are produced by the photodissociation of ozone. The measure of this emission is a direct measure of the photodissociation rate of ozone. When combined with the measurement of the solar flux in the 2000-3000 A region, the airglow measurement may be used as a measure of ozone density. This technique will be useful in the 50-90 km region.

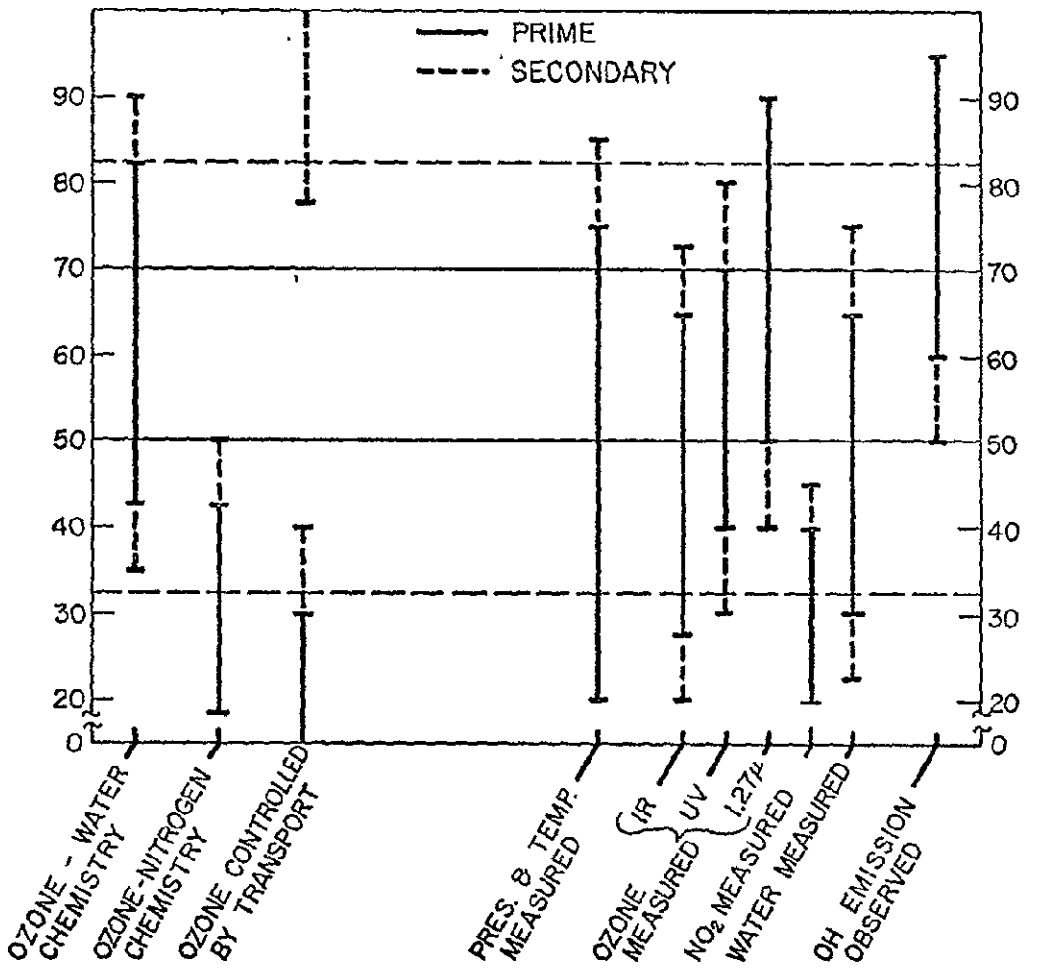

Figure 2.13 Altitude Regions. The first set of bars shows ozone chemistry changes with altitude. The second set shows the range of the instruments; good data can be taken over the region of the solid line and, with some effort, extended into the region of the dashed lines. The prime region for most of the experiments performed will be 50-70 km.

Ozone will also be measured using a limb scanning radiometer which measures emission in the 9.6μ band of ozone. This is thermal emission and is a measure of the cooling due to ozone in this part of the mesosphere. When combined with measurements of the temperature of the atmosphere, the 9.6μ measurement may be used to determine ozone density. This technique will be useful between 25 and 65 km.

The temperature of the atmosphere will be determined by measuring two wavelength intervals in the 15μ band of carbon dioxide. These measurements will be analyzed to determine the temperature and pressure of the mesosphere between 20 and 75 km. Changes in temperature may be the result or the cause of changes in ozone density.

The amount of water vapor between 30 and 65 km will be determined by measuring thermal emission in the 6.3μ band. When combined with temperature measurement, the 6.3μ emission will be a measure of the water vapor density. The ozone density in the 50-70 km region is controlled by the photochemistry of odd hydrogen. The production rate of hydroxyl radicals and atomic hydrogen is determined by the amount of water vapor and by the solar flux at Lyman alpha and between 1700 and 2400 A.

Nitrogen dioxide will be measured between 20 and 40 km using a limb scanning spectrometer. Two wavelengths near 4500 A will be measured simultaneously. The densitites of nitrogen dioxide and ozone are interrelated.

Adel, A., 1951, "Atmospheric Nitrous Oxide and the Nitrogen Cycle," Science 113, 624.

Anderson, G. P., C. A. Barth, F. Cayla, and J. London, 1969, "Satellite Observations of the Vertical Ozone Distribution in the Upper Stratosphere," Ann. Geophys. 25, 314.

Barth, C. A., D. W. Rusch, and A. I. Stewart, 1973, "The UV Nitric Oxide Experiment for Atmophere Explorer," Radio Sci. 8, 379.

Bates, D. R., and P. B. Hays, 1967, "Atmospheric Nitrous Oxide," Planet. Space Sci. 15, 189.

Cicerone, R. J., R. S. Stolarski, and S. Walters, 1974, "Stratospheric Ozone Destruction by Man-Made Chlorofluoromethanes," Science 185, 1165.

Craig, R. A., 1965, The Upper Atmosphere, Academic Press, New York.

Crutzen, P. J., 1971, "Ozone Production Rates in an Oxygen-Hydrogen-Nitrogen Oxide Atmosphere," J. Geophys. Res. 76, 7311.

Crutzen, P. J., 1974, "Estimates of Possible Future Ozone Reductions from Continued Use of Fluoro-chloro-methanes (CF_2Cl_2, $CFCl_3$)," Geophys. Res. Lett. 1, 205.

Crutzen, P. J., I. S. A. Isaksen, and G. C. Reid, 1975, "Solar Proton Events: Stratospheric Sources for Nitric Oxide," Science 189, 457.

Crutzen, P. J., and I. S. A. Isaksen, 1975, "The Impact of the Chlorocarbon Industry on the Ozone Layer," submitted to J. Geophys. Res., August 1975.

Crutzen, P. J., 1976, "Perturbations in Stratospheric Ozone Due to NO_x as Obtained with a Two-Dimensional Model," to be published in Proceedings of 4th CIAP Conference.

Donahue, T. M., B. Guenther, and R. J. Thomas, 1973, "Distributon of Atomic Oxygen in the Upper Atmosphere Deduced from OGO-6 Airglow Observations," J. Geophys. Res. 78, 6662.

Ehhalt, D. H., 1973, "Methane in the Atmosphere. Carbon and the Biosphere," Proceedings of the 24th Brookhaven Symposium in Biology, May 16-18, 1972, Tech. Info. Center of INFSERV, USAEC.

Evans, W. F. J., and E. J. Llewellyn, 1973, "Atomic Hydrogen Concentrations in the Mesosphere and Hydroxyl Emissions," J. Geophys. Res. 75, 323.

Frederick, J., 1975, Ph.D. Thesis, Department of Astro-Geophysics, University of Colorado, Boulder, Colorado.

Gille, J. C., and F. B. House, 1971, "On the Inversion of Limb Radiance Measurements: I. Temperature and Thickness," J. Atmos. Sci. 28, 1427.

Heath, D. F., 1973, "Space Observations on the Variability of the Solar Irradiance in the Near and Far Ultraviolet," J. Geophys. Res. 78, 2779.

Hord, C. W., C. A. Barth, and J. B. Pearce, 1970, "Ultraviolet Spectroscopy Experiment for Mariner Mars 1971," Icarus 12, 63.

Hunt, B. G., 1966, "Photochemistry of Ozone in a Moist Atmosphere," J. Geophys. Res. 71, 1385.

Hunten, D. M., 1954, "A Study of Sodium Twilight I Theory," J. Atmos. Terr. Phys. 5, 44.

Hunten, D. M., and D. F. Strobel, 1974, "Production and Escape of Terrestrial Hydrogen," J. Atmos. Sci. 31, 305.

Johnston, H. S., 1971, "Reduction of Stratospheric Ozone by Nitrogen Oxide Catalysts from Supersonic Transport Exhaust," Science 173, 517.

Johnston, H. S., G. Whitten and J. Birks, 1973, "The Effect of Nuclear Explosions on Stratospheric Nitric Oxide and Ozone," J. Geophys. Res. 78 6107.

Liu, S. C., and T. M. Donahue, 1974, "The Aeronomy of Hydrogen in the Atmosphere of the Earth," J. Atmos. Sci. 31, 1118.

London, J., G. P. Anderson, and J. Frederick, 1972, "The Global Distribution of Atmospheric Ozone Derived from OGO-4 Satellite Observations," Trans. Amer. Geophys. Union 53, 997.

London, J., J. E. Fredrick, and G. P. Anderson, 1976, "Satellite Observations of the Global Distribution of Stratospheric Ozone," submitted to J. Geophys. Res.

Molina, M. J., and F. S. Rowland, 1974, "Stratospheric Sink for Chlorofluoromethanes: Chlorine Atom Catalysed Destruction of Ozone," Nature 249, 810.

National Academy of Science, 1975, "Environmental Impact of Stratospheric Flight," Report of the Climatic Impact Committee, Washington, D. C.

Nicolet, M., 1970, "Ozone and Hydrogen Reactions," Ann. Geophys. 26, 531.

Nicolet, M., 1974, "An Overview of Aeronomic Processes in the Stratosphere and Mesosphere," Can. J. Chem. 52, 1381.

Noxon, J. F., 1975, "Nitrogen Dioxide in the Stratosphere and Troposphere Measured by Ground-based Absorption Spectroscopy," Science, 15 August 1975, pp. 547-549.

Park, J. H., and J. London, 1974, "Ozone Photochemistry and Radiative Heating of the Middle Atmosphere," J. Atmos. Sci. 31, 1898.

Strobel, D. F., 1972, "Minor Neutral Constitutents in the Mesosphere and Lower Thermosphere," Radio Sci. 7, 1.

Thomas, L., and M. R. Bowman, 1972, "The Diurnal Variations of Hydrogen and Oxygen Constituents in the Mesosphere and Lower Thermosphere," J. Atmos. Terr. Phys. 34, 1834.

Thomas, R. J., and T. M. Donahue, 1972, "Analysis of OGO-6 Observations of the OI 5577 A Tropical Nightglow," J. Geophys. Res. 77, 3557.

Vidal-Madjar, A., J. E. Blamont, and B. Phissamay, 1973, "Solar Lyman α Changes and Related Hydrogen Density at the Earth's Exobase," J. Geophys. Res. 78, 1115.

Wallace, L., and D. M. Hunten, 1968, "The Dayglow of the Oxygen A Band," J. Geophys. Res. 73, 4813.

3.0 INSTRUMENT DESCRIPTION

The proposed spacecraft will have a complement of five experiments. Four will view normal to the spacecraft spin axis and will, therefore, scan through the limb twice per spacecraft rotation (an ascending and descending horizon). The field of view of these instruments will sweep through the limb sampling a Δh element at the limb of approximately 3.5 km. Due to the spacecraft rotation, the viewing angle will sweep out a $\Delta\Theta$ of 0.1 degree (corresponding to a Δh of $\sim$3.5 km) every 3.3 msec. By proper choice of instrument gate time or sample interval, it is, therefore, possible to obtain a sample spacing as fine as 3.5 km. (Compare this to an atmospheric scale height of $\sim$7 km in the altitude region 50 km to 70 km.) These four limb scanning instruments will measure all parameters required for our analysis of the ozone photochemistry. Section 3.1 describes the ultraviolet ozone experiment which directly measures the O_3 concentration by the attenuation of Rayleigh scattered solar radiation along the slant path. Section 3.2 describes the four-channel infrared radiometer used to measure temperature-pressure curves in the 50 km to 70 km region. This instrument also measures the H_2O and O_3 concentrations from their thermal emissions along the slant path. The airglow emission between 7000 A and 2.4μ due to $O_2(^1\Delta_g)$, OH, and $O_2(^1\Sigma_g)$ will be measured by the airglow experiment described in Section 3.3. Section 3.4 describes the nitrogen dioxide

experiment which measures absorption just as the ozone experiment but in visible spectral regions.

The fifth instrument is an ultraviolet solar monitor and is described in Section 3.4. Unlike the limb scanning instruments, this experiment has a look direction 45° to the spacecraft rotation axis. In a 3 o'clock orbit the solar instrument will scan through the sun once per spacecraft rotation. The acceptance angle of the solar experiment is ±10°, and, therefore, a reasonable deviation in the orbit will have little impact on the experiment.

The 1/8 meter spectrometer used for all of the above instruments, with the exception of the infrared radiometer, has been flown by this laboratory as experiments on rockets and satellites. All instruments will be built and tested in this laboratory. Since all of the instruments are essentially optical, they will be calibrated for wavelength response, photometric sensitivity, field of view, and off axis scattered light. Special optical testing, such as polarization, will be performed in the event that such effects have an impact on the experiment. All of these calibrations will be performed in this laboratory.

3.1 UV Ozone Experiment

3.1.1 General

The determination of ozone concentrations in the 50 km to 70 km region of the atmosphere will be made by observing the ozone absorption of Rayleigh scattered sunlight at the

limb. The instrument proposed to make these measurements is a small, dual channel Ebert-Fastie spectrometer operating in the spectral range 2460 A to 3350 A. A small telescope will image a delta height element at the limb on the spectrometer entrance slit. As the spacecraft rotates, the field of view will sweep down through the limb, and data will be recorded from 120 km to 20 km minimum ray height. This instrument has 1/8 meter focal length and is the same basic design as one presently being built by this laboratory for use on Pioneer Venus (see Figure 3.1). Similar spectrometers have been flown by this laboratory as sounding rocket experiments on OGO-2 and -4, Mariners 6, 7, and 9, and Atmosphere Explorers-C and -D. They have satisfactorily undergone the full spectrum of environmental testing as well as launch and recovery, and they have proven to be most reliable.

3.1.2 Telescope

The present design for the collecting optics is an f/5, 250 mm focal length Cassegrain telescope. This folded optical layout is compact and lends itself to baffling against off axis light. In the telescope focal plane, 1 mm corresponds to a field of view of 0.23°. The instrument field of view will, therefore, be limited by the spectrometer entrance slit which will be 0.44 mm x 2.50 mm (FOV 0.10° x 1.5°). The telescope aperture will be 5.0 cm x 5.0 cm with an effective collecting area of $\sim$20 cm^2 The primary and secondary optics will be coated with Al-MgF_2.

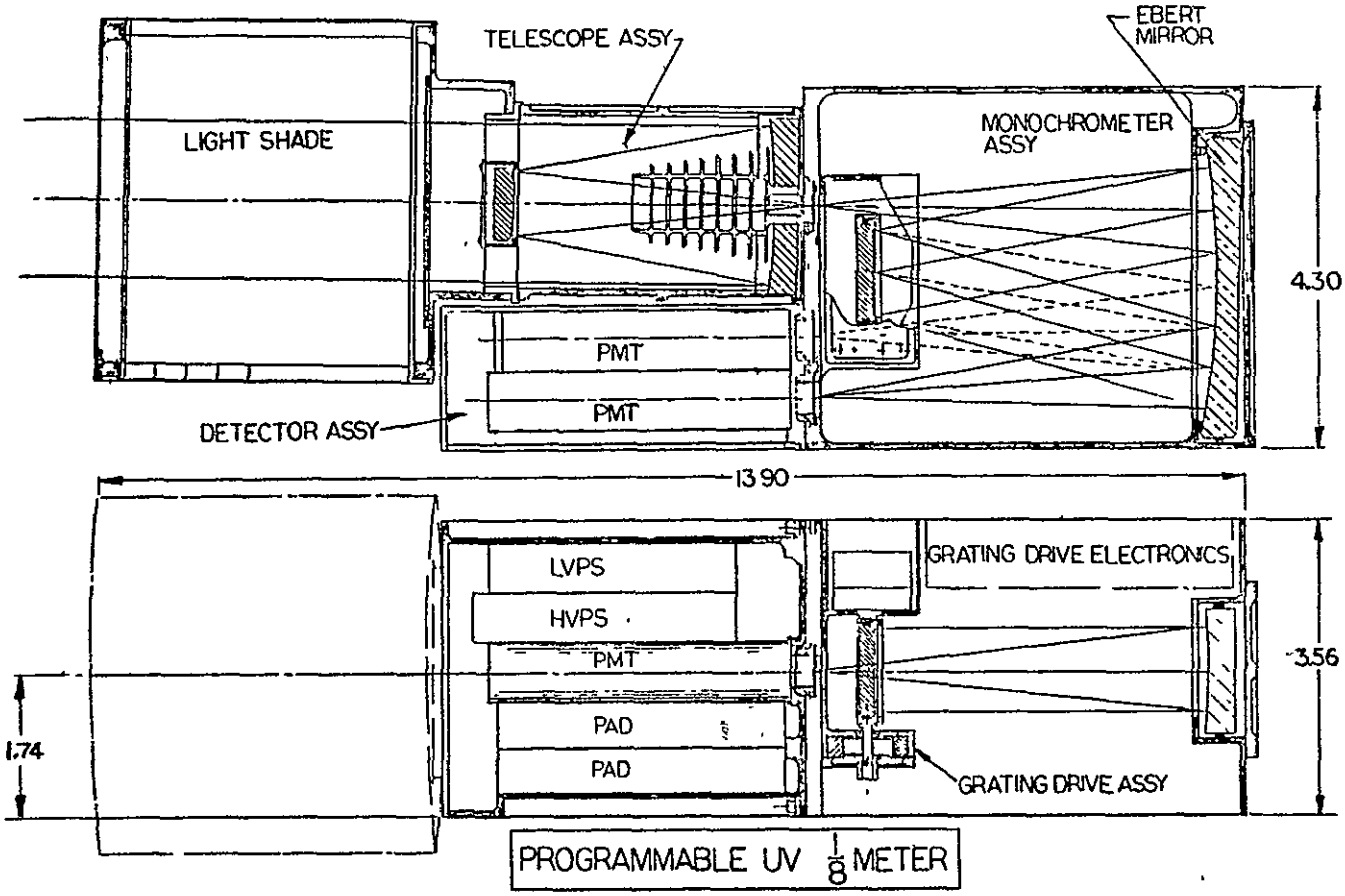

Figure 3.1 Programmable Ultraviolet Spectrometer.

3.1.3 Spectrometer

The spectrometer will be a 1/8 meter, Ebert-Fastie design. Since the Ebert mirror has a focal length of 12.5 cm, a speed of f/5 is achieved by use of a 2.5 cm grating.

The grating will have a ruling density of 3600 lines/mm blazed at 24° (i.e., ∿2400 A). The dispersion at the exit slit is, therefore, approximately 18 A/mm in first order at 2400 A. An exit slit width of 1.7 mm will thus give a trapezoidal spectral response function, FWHM = 30 A. The exit slit length will be determined by the maximum useful photocathode diameter (∿8 mm) and will not stop down the beam; that is, the image height will be determined by the entrance slit length.

There are two exit slits with a spatial separation of 1.4 cm. This corresponds to a spectral separation of approximately 250 A in first order. The grating may be rotated from 26.6° to 34.4° in 64 steps. Each step corresponds to a wavelength shift of 10 A, and the total range covered by Channel A is 2460 A to 3100 A and by Channel B is 2710 A to 3350 A.

3.1.4 Detectors and Sensitivity

Channel A and Channel B will each employ a separate 510F (CsTe with MgF_2 window) photomultiplier with its own associated pulse counting electronics. Maximum count rates

will be recorded near 3100 A when the minimum ray height of the telescope field of view is near 50 km. The signal may be as large as 20 MR (MR = 10^{12} photons cm^{-2} sec^{-1} $(4\pi)^{-1}$) per bandpass of the spectrometer. Since both Channel A and Channel B are capable of operating in this spectral region, they will be designed to have similar sensitivities.

The pulses from the photomultiplier tubes (PMT) are fed through a PAD (Pulse Amplifier and Discriminator) circuit, and the PAD output pulses are about 100 nsec long by 10 volts high. Dead time of this circuit is on the order of 50 nsec, and the circuit will saturate only for count rates greater than 7 MHz. Maximum anticipated signal at the minimum ray height of 50 km is approximately 1.0 MHz. Therefore, no gain control of the PMT is required.

The pulse counters will have programmable gate times of 2 msec, 4 msec, and 8 msec. The count rate is given by:

$$C(\Delta\lambda) = B(\Delta\lambda)\ A_T(A_S/F^2)\ QT$$

where $C(\Delta\lambda)$ is the count rate for spectrometer bandpass $\Delta\lambda$, $B(\Delta\lambda)$ is the Rayleigh scattered brightness for $\Delta\lambda$, A_T is the effective telescope area, A_S is the area of the spectrometer entrance slit, F is the telescope focal length, Q is the quantum efficiency of the detector, and T is the optical transmission of the telescope spectrometer. At

3100 A: $B(\Delta\lambda) = 3.0 \times 10^{13}$ photons cm^{-2} sec^{-1} 30 A^{-1} $(4\pi)^{-1}$; Q(3100 A) = 0.0075 count/photon; T(3100 A) = 0.08; A_τ = 20 cm^2; $A_s = 2.86 \times 10^{-2}$ cm^{-2}; F = 25.0 cm.

$$C(30\ A) = 1.3 \times 10^6 \text{ counts/sec.}$$

The accumulated counts per gate time, therefore, varies from 2600 counts to 10,500 counts. Minimum count rates should be a few counts per gate time. Dark counts will contribute less than one count per gate time.

3.1.5 Data and Telemetry

The timing of limb data from the UV ozone experiment is keyed from the limb crossing sensor. By knowing the rate of spacecraft rotation and the angle between the limb crossing sensor and the FOV of this experiment, it will be possible to time the start of data accumulation to within 1.0 msec. Data from the 20 gate times following start of experiment will be telemetered for both Channel A and Channel B. Assuming a spacecraft altitude of 400 km and a rotation rate of 5 revolutions per minute, the spacecraft field of view will scan through a vertical height at the limb of 43 km, 85 km, or 170 km, depending on the gate time chosen. For example, for a 2 msec gate time, the experiment may be timed to start at an altitude of 80 km $\pm$1 km. Twenty data points will then be taken between 80 km and 37 km with a vertical

separation of 2.0 km. (The vertical field of view of the instrument corresponds to approximately 3.5 km at the limb).

Figure 2.8 is a sample of the type of data which might be expected using a 4 msec gate time with Channel A at 2550 A and Channel B at 3100 A.

3.1.6 Commands and Modes of Operation

Figure 3.2 is a schematic block diagram of the UV ozone experiments electronics. The mode of operation of the UV ozone experiment will be specified by the following commands. Two data bits will be used to specify the gate time; possible gate times are 2, 4, and 8 milliseconds. Fourteen bits will be required to specify the time of data start. This gives a maximum time from the limb crossing signal of 16 seconds as measured by the 1.0 millisecond clock. The period of spacecraft rotation is approximately 12 seconds.

One bit will be used to specify which of two types of experiment is to be run. The first type is a scanning mode in which the wavelength drive is initiated to the low wavelength limit and then increments one step per spacecraft rotation. In this manner a full spectrum between 2400 A and 3500 A is obtained in 64 spacecraft rotations, that is, once every 12.8 min. The second type of experiment is a fixed wavelength mode and must be accompanied by six bits of wavelength drive information. In this mode the drive slews to one of the 64 wavelength positions and remains at that

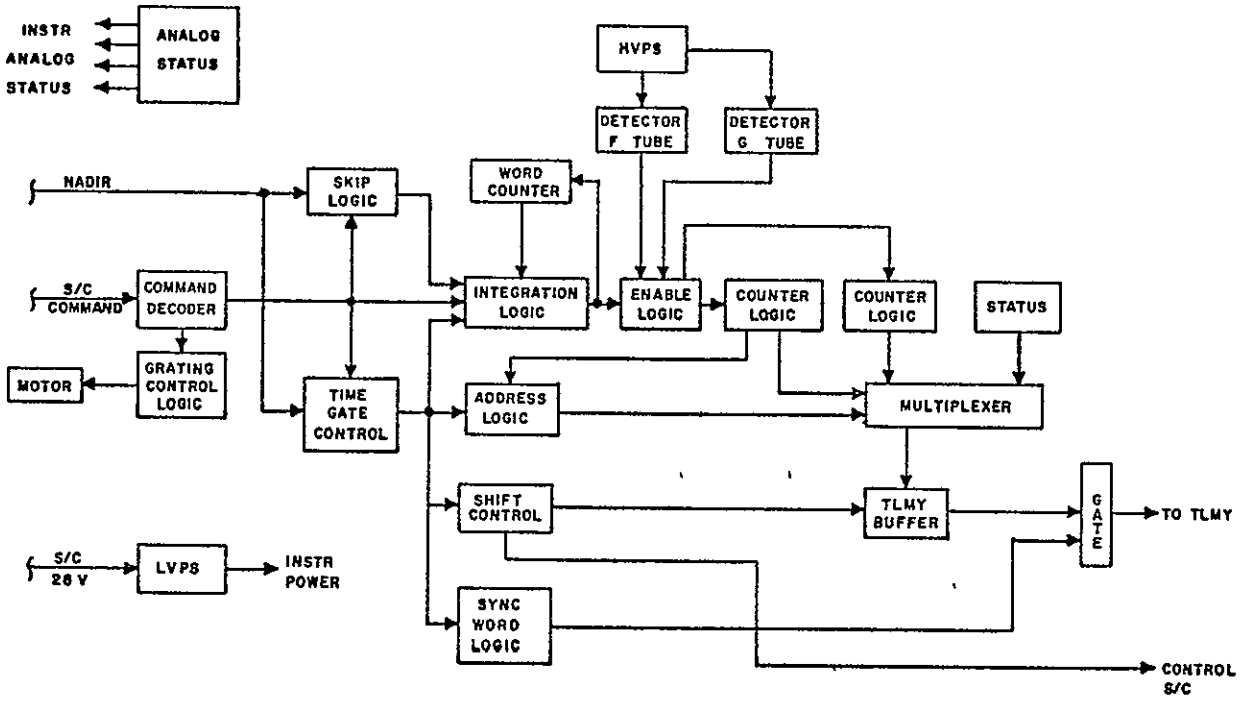

Figure 3.2 Ultraviolet Ozone Instrument Block Diagram

position until another mode command is received. The ozone profiles will be obtained by operating in this mode; and, by programming different wavelengths, it will be possible to probe different depths in the atmosphere.

3.1.7 Instrument Physical Characteristics

Weight	Spectrometer	3.5 lbs
	Logic	2.0 lbs
	Telescope	0.5 lbs
	Total	6.0 lbs
Size	Spectrometer, 10½" x 5½" x 4½"	
	Spectrometer and Telescope, 14" x 6" x 4½"	
Power	1.5 watt	
Telemetry	40 data words per spacecraft rotation	
Duty Cycle	from 0.40 sec to 1.60 sec per spacecraft rotation	
Command	two command words	
Pointing Requirements	Spin axis must be parallel to the limb to ±3°	

3.2 Four-Channel Infrared Radiometer

3.2.1 General

Radiance measurements at four wavelengths in the infrared are achieved with a Cassegrain telescope system using passive, radiatively cooled, mercury-cadmium telluride detectors. The instrument field of view defines a region of atmosphere about 3.5 km in height. Data are taken at a rate

to give one data word per instantaneous field of view, IFOV, as the IFOV sweeps through a 4 degree angle that is equivalent to a limb scan from 150 to 20 km in altitude. Each channel is sampled 20 times per spacecraft rotation.

The instrument makes temperature measurements by viewing carbon dioxide emission with narrow and wide spectral bandwidth channels centered at 15.5 μ. Ozone and water emissions are measured at 9.6μ and 6.3μ, respectively.

3.2.2 Optical System

As presently conceived, the telescope has a 7 inch clear aperture, a f/1.2 primary mirror, and a secondary mirror with magnification of 1.5 to give an effective f number for the system of f/1.8. The field stop is a mask which defines identical 0.1° x 0.40° fields of view for each channel. A layout of the experiment is shown in Figure 3.3. At the focal plane each field stop is 0.022 x 0.088 in^2 and is arranged so that the narrow dimension is along the direction of sweep. A temperature controlled, black body calibration source will rotate into the field of view. Calibration will be done once every five rotations of the satellite or about once per minute.

At the system focal plane a vibrating reed chopper chops the beam by interposing a mask similar to the field stop whose total displacement is slightly larger than 0.024 in. A chopping frequency of 10^3 Hz can be achieved, using a chopper such as Bulova L40C.

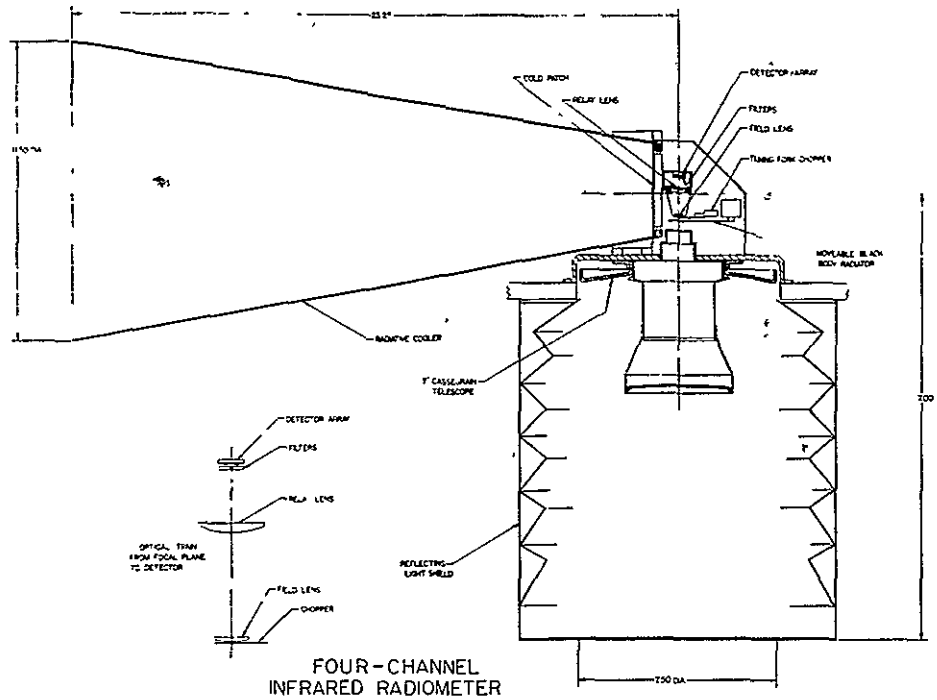

Figure 3.3a

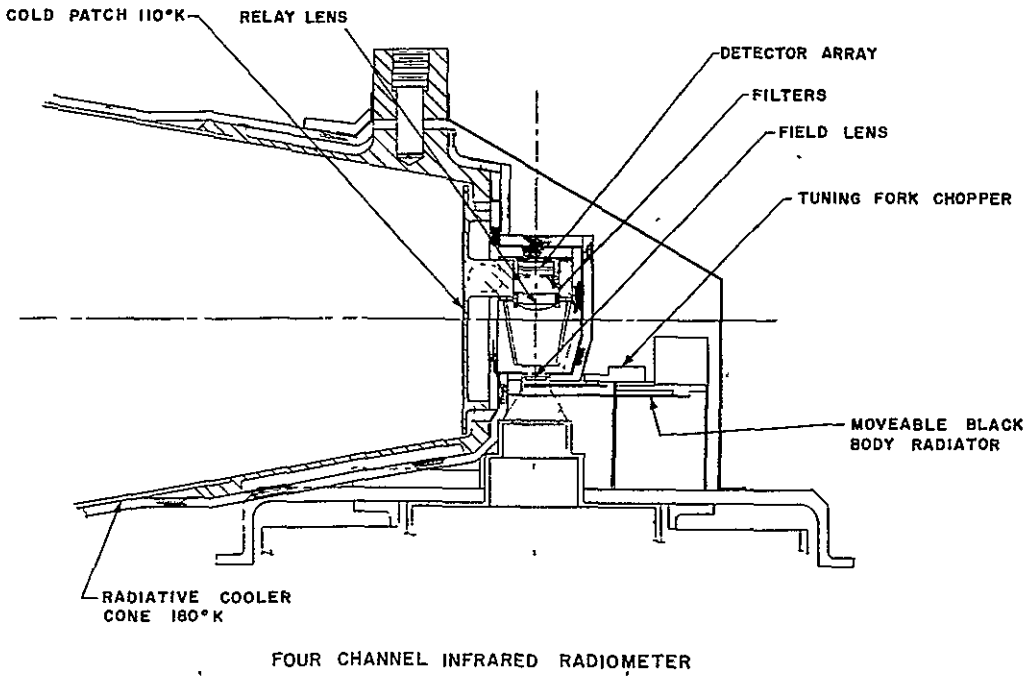

Figure 3.3b

A set of germanium lenses focuses the field stop onto the detectors. Each (Hg-Cd)Te detector is individually connected to the radiatively cooled patch. The detector description is given in Section 3.2.4. Immediately in front of each detector, or deposited on it, is the proper bandpass filter.

Crucial to the optics system design is the rejection of off axis radiation. Since this system scans into regions of ever increasing radiance, the narrow field information must not be compromised by scattered radiation from brighter elements. The off axis rejection should be at least 10^{-4} at 1.5° from the optic axis. Low reflectance materials, black velvet (3M), and appropriate baffling will reduce multiple scattering. Spectral baffling will be used to reject light and heat.

3.2.3 Passive Radiative Cooler

The detectors must be cooled to operate properly. Two suitable means of cooling on a spacecraft are solid cryogenic coolers and passive radiators. Solid cryogenic coolers produce colder temperatures but are more massive and expensive than passive radiative coolers. They also have a functional life of one year or less. We have chosen the passive cooler to provide suitable operating temperatures. The radiative cooler operates by allowing a disk to radiate its energy into deep space while minimizing its heat loads. Surrounding the disk is a highly reflective cone that

shields the disk from high temperature objects, such as the earth. To reduce radiative heat transfer between the cone and the disk, the cone is cooled by attaching it to an unshielded cooler plate.

The cone, with a half angle of 9° and half-cone viewing angle of about 18°, is mounted on the end of the spacecraft always pointed away from the sun and will look at deep space and not see the earth. The cooler is essentially two-stage, consisting of a radiating disk at the bottom of a cone 20.2 inches long whose outer aperture is 10.5 inches in diameter and necks down to a 3.4 inch diameter inner aperture. At the inner aperture, there is a radiative cold disk upon which the hermetically sealed detectors are mounted. The primary cooler, located around the horn mouth, cools the horn to about 180 °K.

By carefully isolating the cooler from the spacecraft, the cooler will radiate a total power load as shown in Figure 3.4. The thermal equilibrium temperature of the patch is given for the total power load on the patch. The total power load includes parasitic heat leaks from insulation, wires, etc., from detector power dissipation, and from radiated input, both signal and background. Optimum detector mounting and wire sizing and routing constitute a major instrument design task.

During the first two weeks after launch, the cooler is heated by heater wires in the horn, to prevent condensation

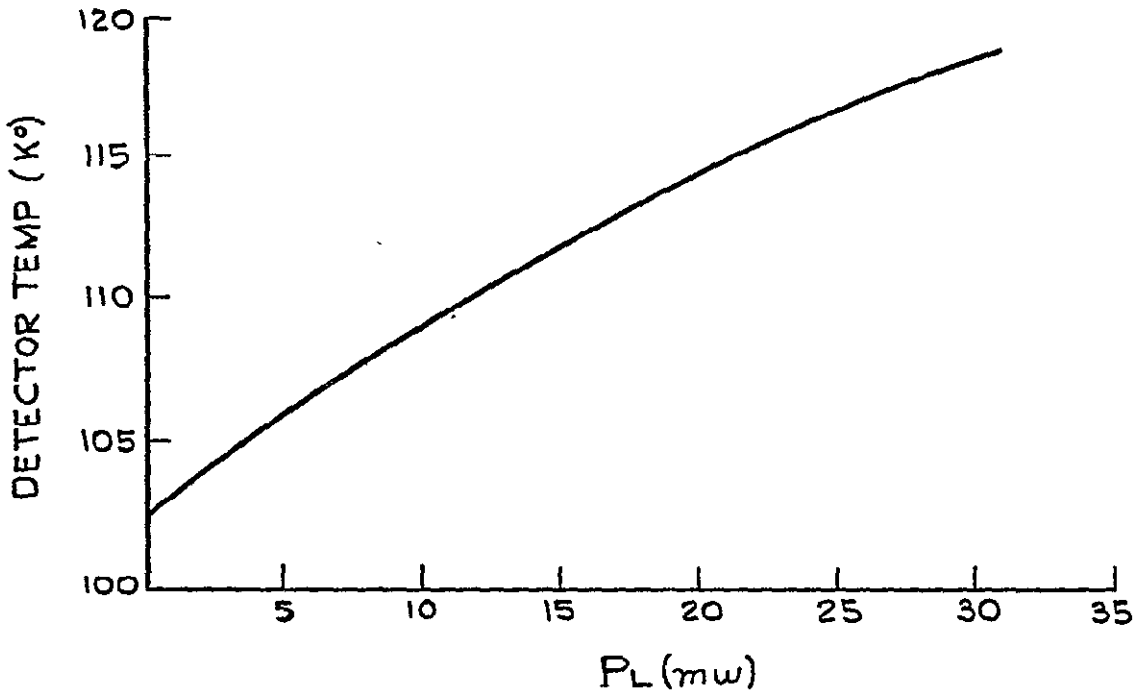

TOTAL THERMAL LOAD VS.
OPERATING TEMP

Figure 3.4

on its surfaces as the satellite outgasses. This will be aided by a protective cover to be blown off after satellite orientation and outgassing. This cover will also protect the cooler from direct sunlight during orbit injection.

A preliminary analysis and design study of the cooler was done by Annable at ITT. We have modified that study to accept conditions of a higher orbit and to include heating of the cold disk by the earth through reflections off the cone. Since this heating is a function of the spacecraft altitude, the analysis will use the lowest expected orbit, 400 x 600 km. In order to simplify the calculations, we assume the spacecraft spends 25% of its time at 400 km, 50% at 500 km, and 25% at 600 km. Assuming no heat load, the temperature of the outside or primary cooler is given by

$$\varepsilon_a \sigma T_a^4 = F_{ae}(\varepsilon_a W_{ir} + \alpha_a W_s \cos 45°)$$

$$= 20.3\ F_{ae}\ \text{mw cm}^{-2}$$

where $\varepsilon_a = 0.85$, $\alpha_a = 0.20$, and W_{ir} and W_s are the infrared and reflected solar radiation from the earth. F_{ae} is the fraction of the primary cooler's field of view (or any vertical flat plate) that contains the earth and is given by

$$F_{ae} = \frac{1}{\pi}(\beta - \sin\beta \cos\beta)$$

where β is the angle between the earth's horizon and its center. The values are given in Table 3.1. The average for the orbit implies a temperature of 176 °K. The cone which is attached to this cooler will probably be 180 °K or less.

The cold disk to which the detectors are attached has the following power loads.

conduction	4.4 mw
cone wall coupling	19.0 mw
Earth coupling by reflection	13.2 mw
Optical port	3.0 mw
TOTAL	39.6 mw

Since the disk's area is 58.8 cm^2, the power load implies a temperature of 104.4 °K. The conduction and cone wall coupling loads were estimated by ITT. The cone wall coupling estimate assumes a cone emittance of 0.04 and an average of 1.2 reflections. Because of the narrow cone angle this estimate is uncertain and needs further study.

We estimate the optical port load by assuming a low emittance mask slightly larger than the field of view directly behind the warm lens. The load was calculated assuming an aperture of 0.1 cm^2, an emittance of 1, and an effective temperature of 295 °K.

The heating by earth reflected radiation was estimated assuming 100% reflection. Using cone optics the field of view factor F_{be} numerically calculated is shown in Table 3.1.

Table 3-1

Altitude	β	F_{ae}	F_{be}
400	70.3°	0.289	0.262
500	68.1°	0.268	0.122
600	66.1°	0.249	0.0048
Ave.	--	0.2685	0.0138

To estimate the heat load a factor of 0.8 was put in as an estimate for multiple reflection effects. A higher orbit would decrease the two largest power loads.

Not included in the power loads is detector biasing. We hope to bias the detectors only while data are being taken -- about 1% of the time. By replacing every fifth data-taking period with a calibration cycle of the same length, drifts should be small and measured.

3.2.4 Detectors

The four channels use mercury-cadmium telluride, (Hg-Cd)Te, detectors with bandpass filters. The germanium lenses that focus the field stop onto the detector plane have a magnification of 1/1.82. The detector active area is 0.012 x 0.048 in^2 for each channel. Larger demagnification results in high angles of incidence on the detectors and is detrimental to the filter operation.

Each detector will be chosen to have a specific detectivity, D*, having a maximum for the center wavelength. Figure 3.5 presents a family of detector curves of D* versus

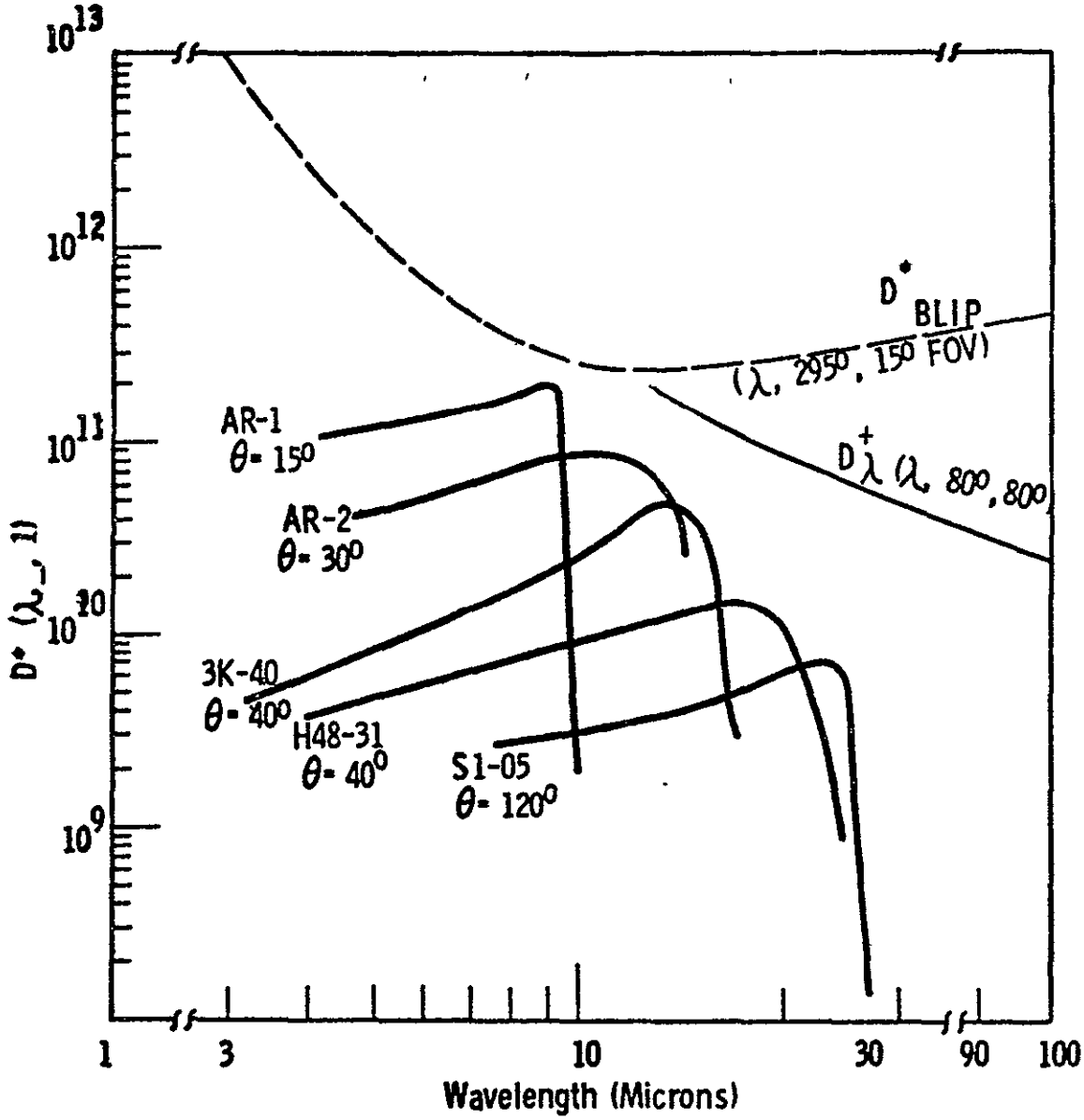

Figure 3.5 Family of (Hg,Cd)Te Photoconductors.
Operating Temperature = 77 °K

wavelength at liquid nitrogen temperature while Figure 3.6 shows the temperature characteristics of (Hg-Cd)Te detectors. The cold patch temperature will be about 105° to 115° K. This is suitable for all detectors. Compared to liquid nitrogen temperatures where these detectors are usually operated, the 15μ channel has the greatest reduction of sensitivity. Fortunately, 15μ is also the strongest signal.

Another detector sensitivity factor is related to the chopping frequency used. Because of the 1/f noise, (Hg-Cd)Te detectors are typically chopped at above 1 kHz. For 2 to 3 kHz, the D* could decline by a factor of around 2, depending on the detector.

Each detector will have a bandpass filter placed directly over it, forming a detector filter unit. Each detector unit is mounted on the cold patch in such a way that the optical cross-talk between units is made negligible. The four detectors are sealed in an evacuated chamber with the lens forming the window. The field lens temperature will be between the temperatures of the cold patch and the instrument housing. Thermal design will make this temperature high enough so that outgassing will not condense on the field lens.

The bandpass filters, lenses and detectors will be antireflectance coated to increase sensitivity. Each detector unit will be optically baffled from the others to increase the isolation between them.

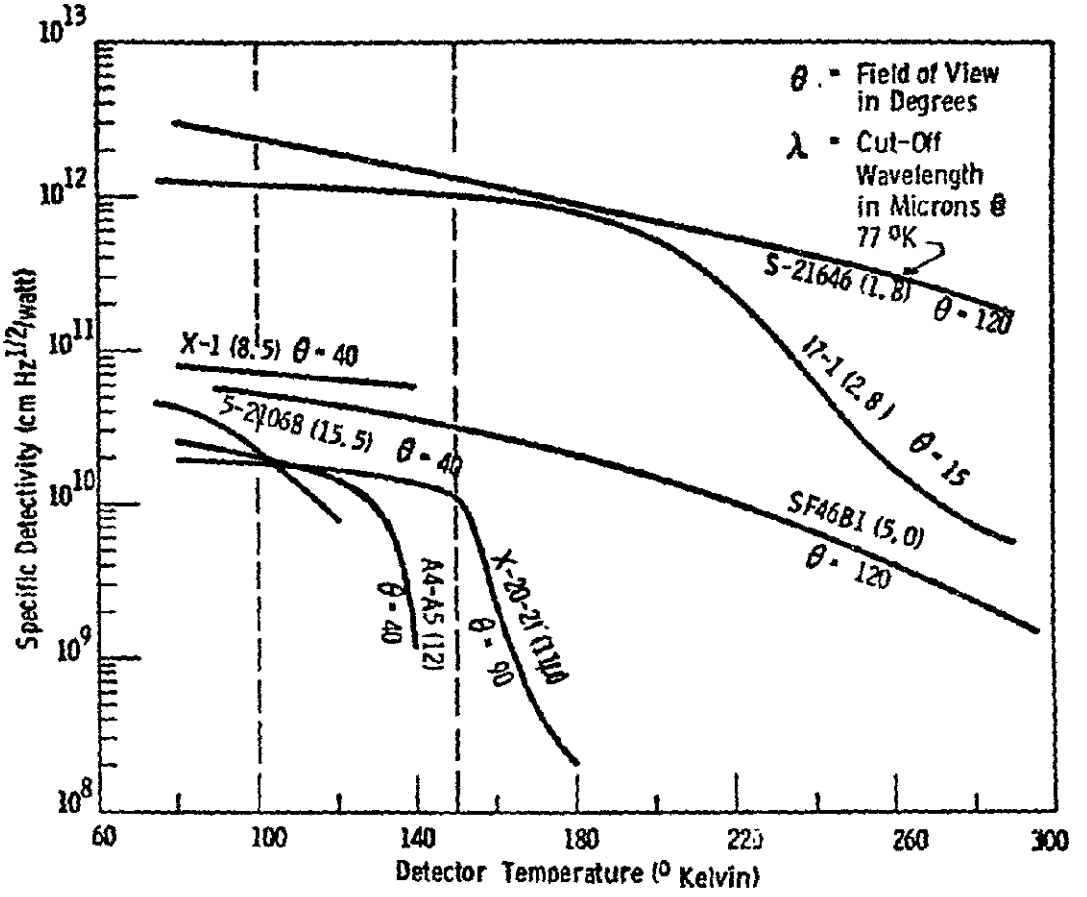

Figure 3.6 Temperature Dependent Behavior of (Hg,Cd)Te Photodetectors

The following table (3-2) presents the instrument sensitivity in terms of noise equivalent radiance (NEN) for a 7-inch aperture with 35% obscuration, an optics transmission and electronics efficiency of 65%, and a 0.1° x 0.4° instantaneous field of view (IFOV). Also assumed is a 0.012 x 0.048 in^2 detector and an electrical bandwidth given by the Nyquist criterion: the bandwidth must be greater than 1/(2t) where t is the time to sweep one IFOV (about 3.3 ms) and where one data sample is determined for each IFOV. An electrical bandwidth of 151 Hz centered at the chopping frequency is needed. The D* values are extrapolated estimates assuming a 110 °K detector operating temperature. These estimates are realistic, or even pessimistic, based on data from manufacturers and from the LRIR of NIMBUS. The effect of changes of D*s and NEN can be estimated using the figures in the next subsection. To set gain levels and to know accurately the dynamic range of the instrument, a radiometric calibration of the optics-detector system will be made. The proper operation of the instrument electronics and optical system must be tested for linearity and gain switching. In particular, the modulation transfer function of the instrument must be accurately measured. The spectral response of each component and the total system will be measured.

Table 3-2

Channel			D* cm $H_3^{1/2}W^{-1}$	NEN Wm^{-2} st^{-1}
1	15.5 μ 645 cm^{-1}	17.2-13.2 μ 590-760 cm^{-1}	$7x10^9$	0.004
2	15.5 μ 645 cm^{-1}	15.7-14.7 μ 635-680 cm^{-1}	$7x10^9$	0.004
3	9.6 μ 1042 cm^{-1}	10.6-8.6 μ 940-1155 cm^{-1}	$1.4x10^{10}$	0.002
4	6.3 μ 1587 cm^{-1}	7.2-6.1 μ 1380-1640 cm^{-1}	$2.8x10^{10}$	0.001

$NEN = \sqrt{A_D \Delta F}/D^* \Omega A_o T_o T_P T_c T_T$

For all detectors:

$A_o = 248.2\ cm^2$	7" Dis primary
$T_T = 0.65$	Due to 4.1" secondary
$\Omega = 1.22 \times 10^{-5} SR$	0.1° x 0.4°
$A_D = 3.7 \times 10^{-3} cm^2$	0.012" x 0.048"
$T_o = 0.65$	2 mirrors at 0.95 and 3 lenses at 0.90
$T_F = 0.80$	Filter
$T_c = 0.26$	Sine wave chopper
$\Delta F = 151$ Hz	

3.2.5 Expected Radiance

Expected radiances for each of the channels have been calculated for a variety of climatological situations and compared to the expected noise equivalent radiances. For the CO_2 channels, Figures 3.7 and 3.8, signal-to-noise ratios greater than one can be expected over the entire region of the experiment. The lowest signals occur for cold mesopause situations. The signal-to-noise ratio for the ozone channel (Figure 3.9) reaches one at about 75 km for most atmospheric cases but occasionally at 70 km in cold mesopause regions. The water vapor channel (Figure 3.10) reaches the noise level at about 76 km. The presence of high clouds can produce larger radiance in the wide CO_2, ozone, and water vapor channels. The narrow CO_2 channel is opaque to all but nacreous clouds.

3.2.6 Data Handling

The (Hg-Cd)Te detectors are operated in the photoconductive mode. The magnitude of the output voltage signal is the product of the bias current and the incremental resistance change of the detector due to radiant energy impinging on the sensitive surface. To maximize the sensitivity, the proper bias current must be applied, and a pre-amplifier with high input impedance must be used.

The chopped output signal is fed to a phase sensitive detection system which amplifies, demodulates, and inte-

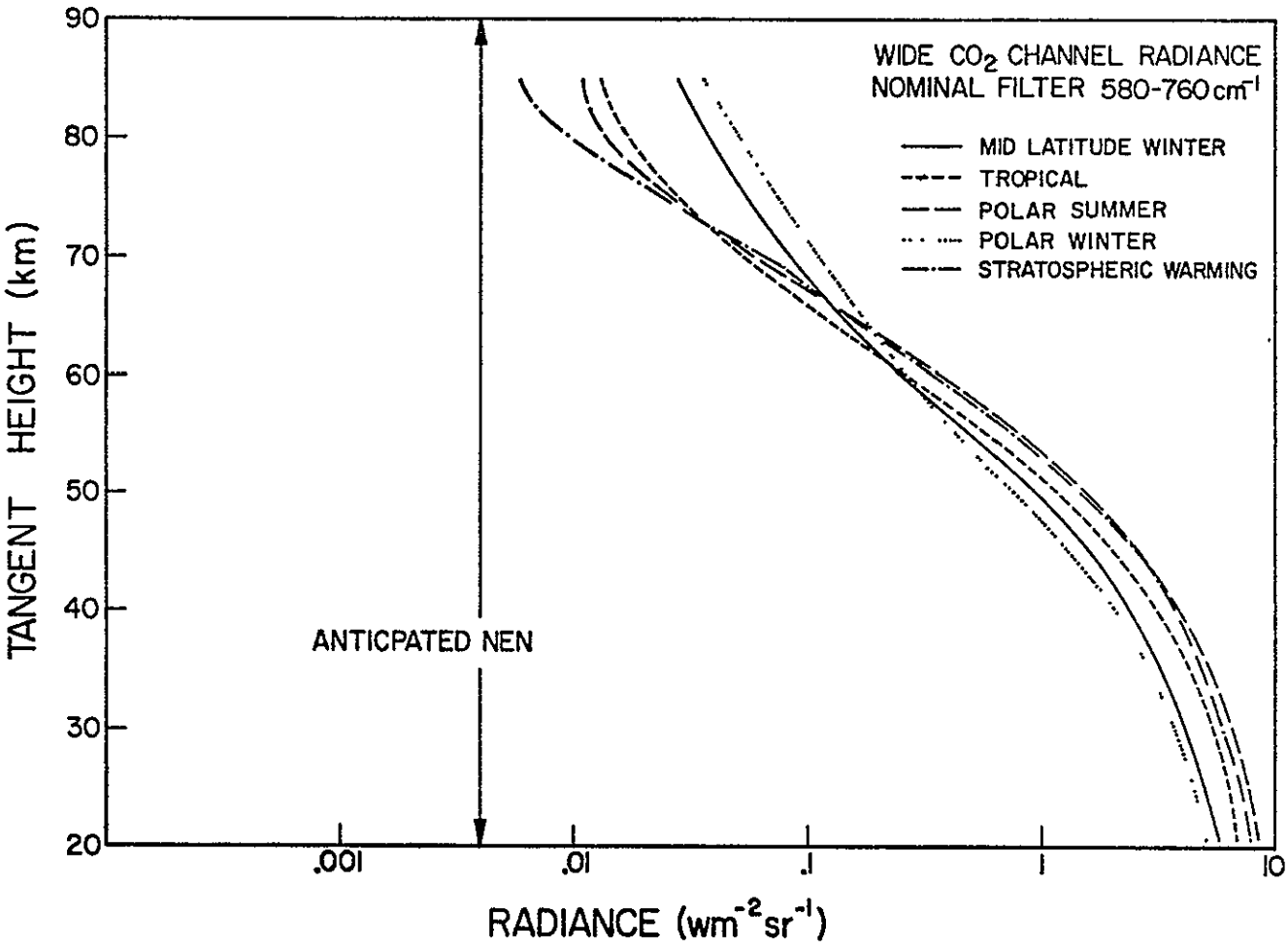

Figure 3.7 Expected radiance for the wide CO_2 channel for a variety of climatological conditions. Even an increase of NEN by a factor of 10 would not seriously affect the data.

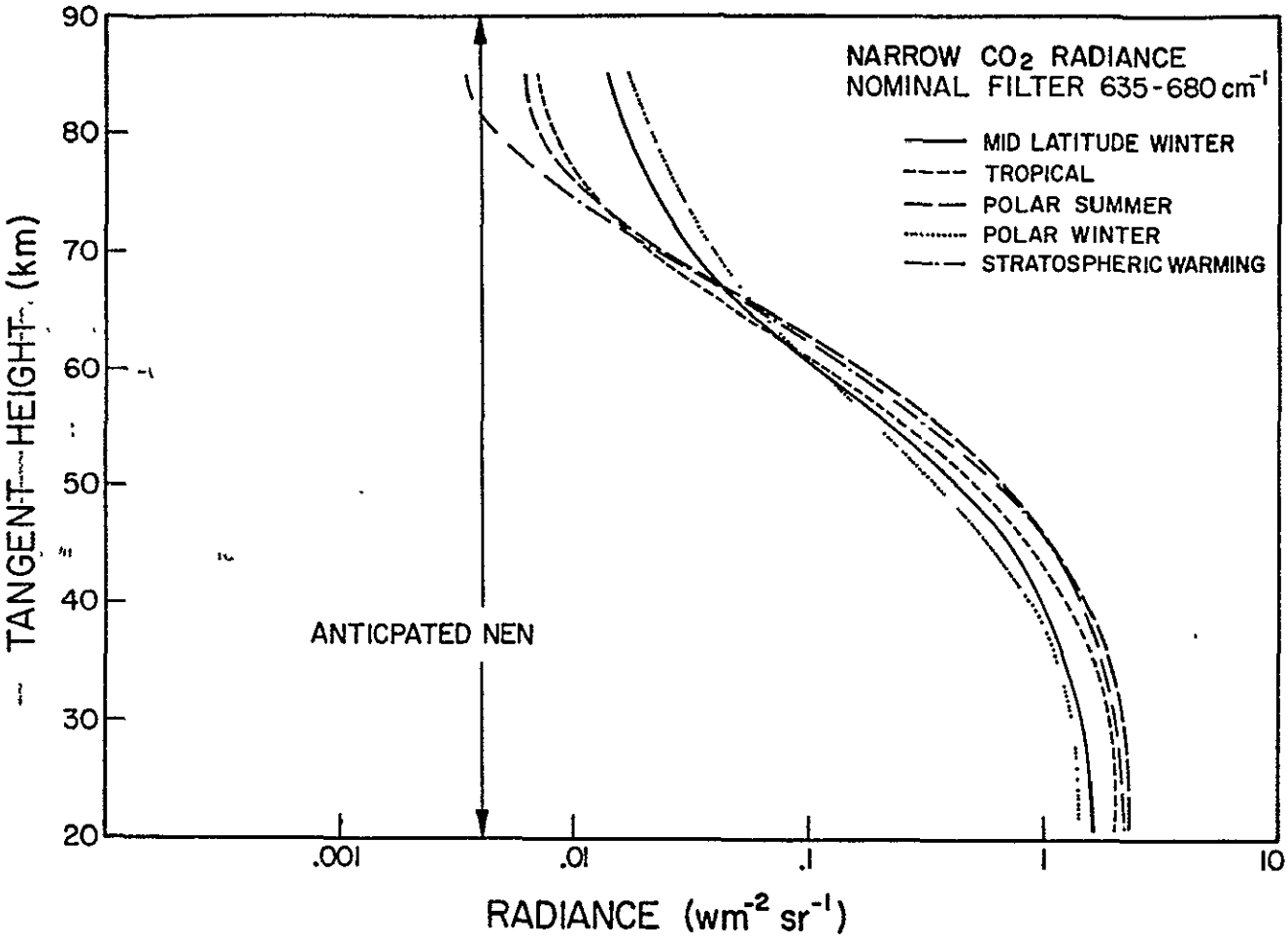

Figure 3.8 Expected radiance for the narrow CO_2 channel.

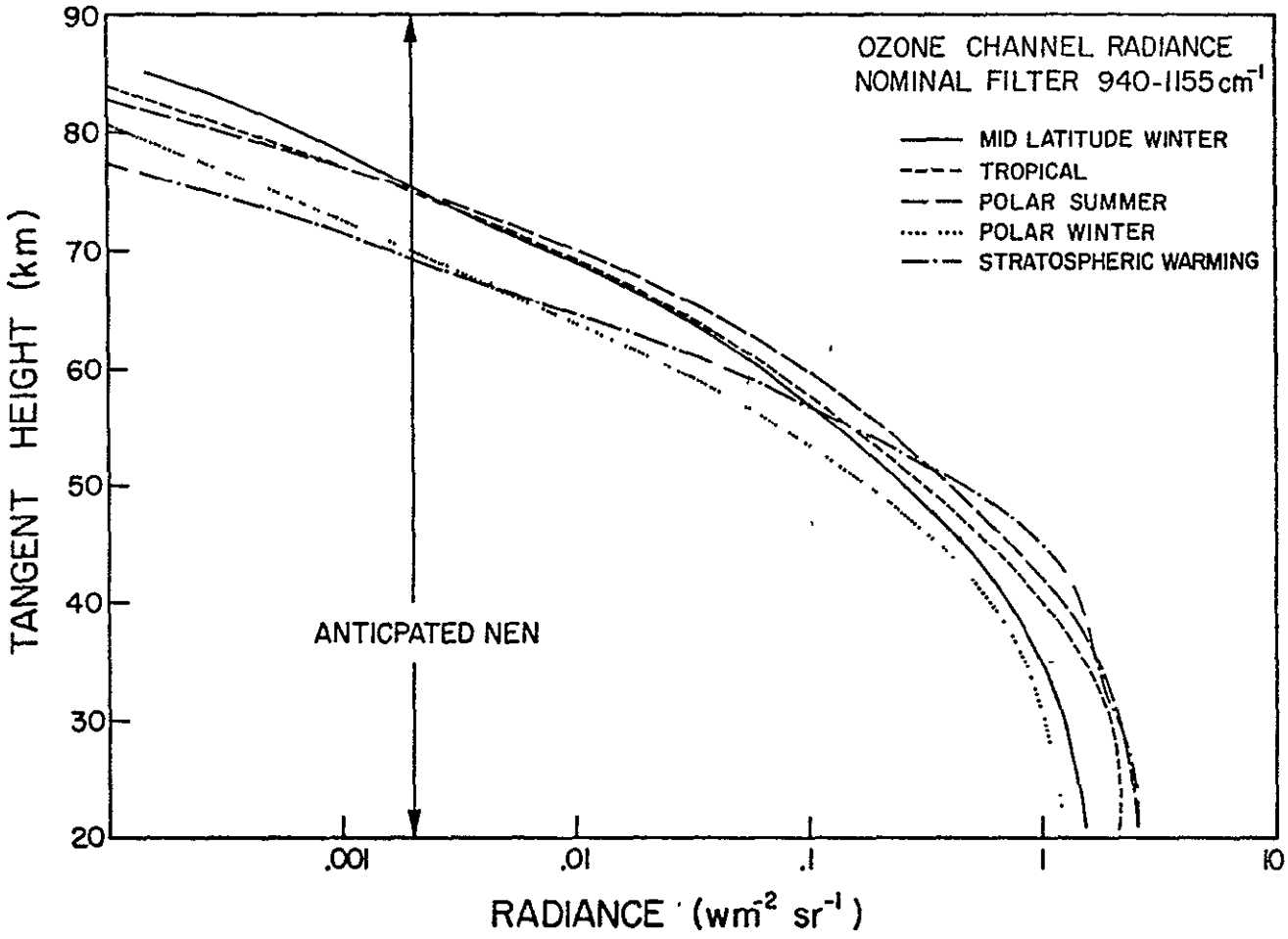

Figure 3.9 Expected ozone radiance.

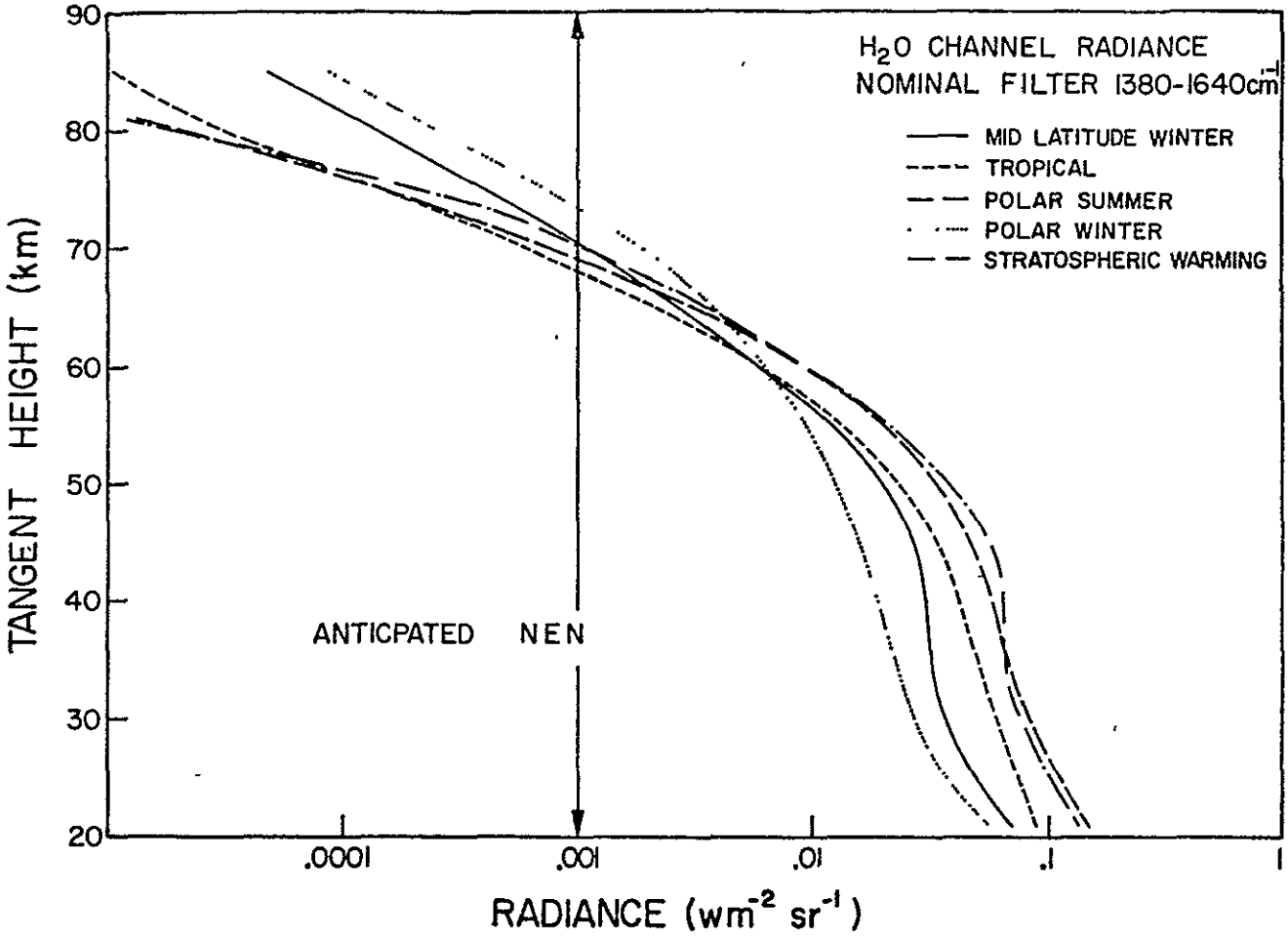

Figure 3.10 Expected water vapor radiance.

grates the AC signal. The DC output is produced proportionally to the amplitude of the fundamental component of the signal. This detection scheme produces an output signal derived from a selectable bandwidth AC signal centered at the chopping frequency. Sample and hold circuits retain the output DC signal until they may be interrogated by an A/D converter.

Gain switching in the main amplifier of the phase sensitive detection system may be necessary to measure the signal dynamic range between the noise of the system and the black body calibration source. Sixteen-bit data words are used, and when in the high gain mode noise level the detector will have one or two bit resolution.

During every spacecraft rotation the four detectors sweep through a 5 degree region of interest. Data are taken at 3.3 ms intervals, giving 20 words per channel for the 5 degree region. The start of data taking is referenced to a nadir pulse. Commandable update of the time from nadir to the start of data taking is possible. Two additional data words per channel are taken each rotation when the IFOV is sufficiently off the limb of the earth (>200 km) to give a reference background observation. Every fifth spacecraft rotation a black body is rotated into view for the reference black body calibration source. In Figure 3.11 the system block diagram is shown.

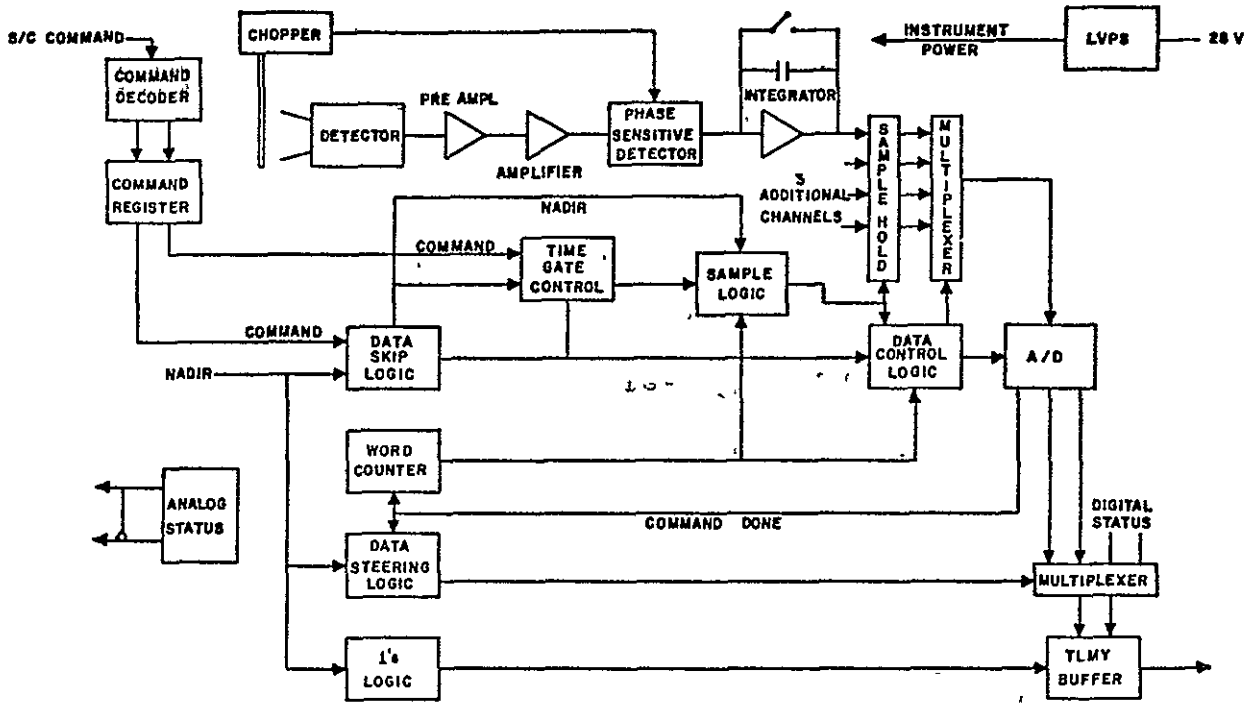

Figure 3.11 Four-Channel Infrared Radiometer Block Diagram

3.2.7 Instrument Physical Characteristics

Weight	Telescope	5 lbs
	Cooler	10 lbs
	Electronics	5 lbs
Power	4 watts	
Size	Telescope	7 inch aperture
	Cooler	10-1/2 inch aperture
Telemetry	88 data words per spacecraft rotation. Each instrument samples every 3.3 ms, 20 words in succession with commandable start from nadir reference. Two words taken off of limb.	
Command	Two command words, 16 bits each required	
	1. Data Skip	
	2. 20 word sequence start time	
	3. Two word sequence start time	
Pointing Requirements	Spin axis must be parallel to limb within ± 1 degree	

3.3 1.27μ Airglow Instrument

3.3.1 General

The photolytic loss of ozone results in excitation of $O_2(^1\Delta_g)$. The $O_2(^1\Delta_g)$ then radiates at 1.27μ to the ground state ($^3\Sigma_g$). By limb scanning at 1.27μ with the airglow instrument, the altitude profile of ozone photolysis is determined. This is easily done by using a grating spectrometer and an uncooled detector system with a narrow field of view (see Figure 3.12).

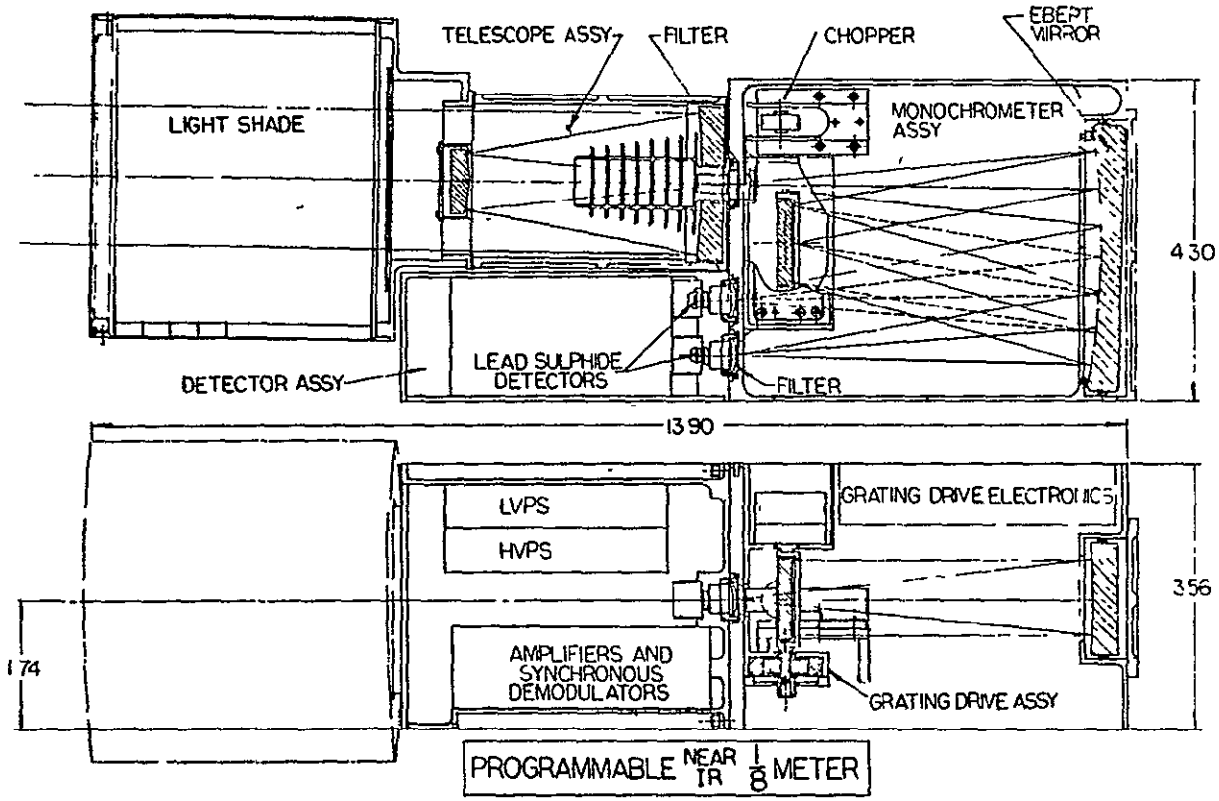

Figure 3.12

3.3.2 Optical System

The programmable Ebert-Fastie spectrometer (Figure 3.12) is the same basic design used for the UV ozone experiment and the solar UV monitor. It is described in Section 3.1. The telescope entrance slit and Ebert mirror will be the same but with optical coating maximized for the near infrared. The grating will have a ruling density of 600 lines/mm blazed at 1.25μ. The dispersion at the exit slit is about 100 A/mm. The exit slit is about 0.7 mm wide and gives a trapezoidal response function FWHM = 70 A. This will match the $O_2(^1\Delta_g)$ emission at 1.27μ. The relay lens behind the exit slit increases the effective speed from f/5 to f/1, which decreases the detector size to 1.5 x 0.16 mm.

At the entrance slit the signal is chopped, and wavelengths short of 7000 A are blocked with a filter. Since the spectrometer has two exit slits, both will be used to give redundancy to the 1.27μ measurement. Using the first slit, wavelengths from 0.7 to 1.4μ can be observed. At the second slit another filter will block light short of 1.2μ; observations from 1.2 to 2.4μ will be made.

The spectrometer is identical to the two others on the satellite. By slowly scanning we can locate the best grating position for observing the 1.27μ band without obtaining signals from the nearby OH (8-5) bands. Grating and detector changes can be deduced and accounted for during flight. In addition, airglow in the mesosphere from OH and

$O_2(^1\Sigma_g)$ can be observed. The sensitivity of the instrument is shown in Table 3-3. The lowest expected slant signal between 80 and 90 km is 25 MR or about 3.13 x 10^7 watts sr^1 cm^2. This gives a signal-to-noise ratio of about 3. Thus, we can expect useable data (especially if averaging several scans) to over 90 km.

TABLE 3-3

SPECTROPHOTOMETER

A_o (Collecting area)	20 cm^2
Ω (0.1° x 1°)	3.05×10^{-5}
D* (300 °K)	8×10^{10}
Δf (same as four channel instrument)	151 Hz
T_o (mirrors) (lenses)	0.8 four each 0.9 one each
T_f (filter and grating)	0.5
T_c (chopper)	0.31
A_D (detector)	$2.56 \times 10^{-3} cm^2$
NEN	11.4×10^{-8}

3.3.3 Electronics

The detector signals will be synchronously demodulated to remove the chopped signal. To cover the full dynamic range of the detector, we will use a four range, auto switching amplifier. The output will be digitally coded

into an 8 bit word. The range will be contained in two bits and the signal in the other six. The compression error produced is 1.5%.

3.3.4 Data and Telemetry

Figure 3.13 is a schematic block diagram of the airglow experiment electronics. The limb data will be timed in a manner similar to the ultraviolet ozone experiment. The data will be sampled for twenty programmable gate times of 2, 4, or 8 msec. For a spacecraft spin rate of five revolutions per minute and 2 msec gate times, data samples are separated by about 2 km at the limb. The expected emission from the slant column will increase from 25 MR at 90 km to 375 MR at 50 km.

3.3.5 Commands

Two bits of command information will be required to set the experiment gate time. This instrument is similar to the other limb scanning instruments in that its timing is keyed from the limb cross signal. Therefore, another 14 bits will be required to set the "experiment start" register. Using three command bits, the airglow experiment will also be programmed to transmit data every nth spin, where n = 1, 2, 4, 8. Commands for a spectrometer would be the same as those described in Section 3.1.

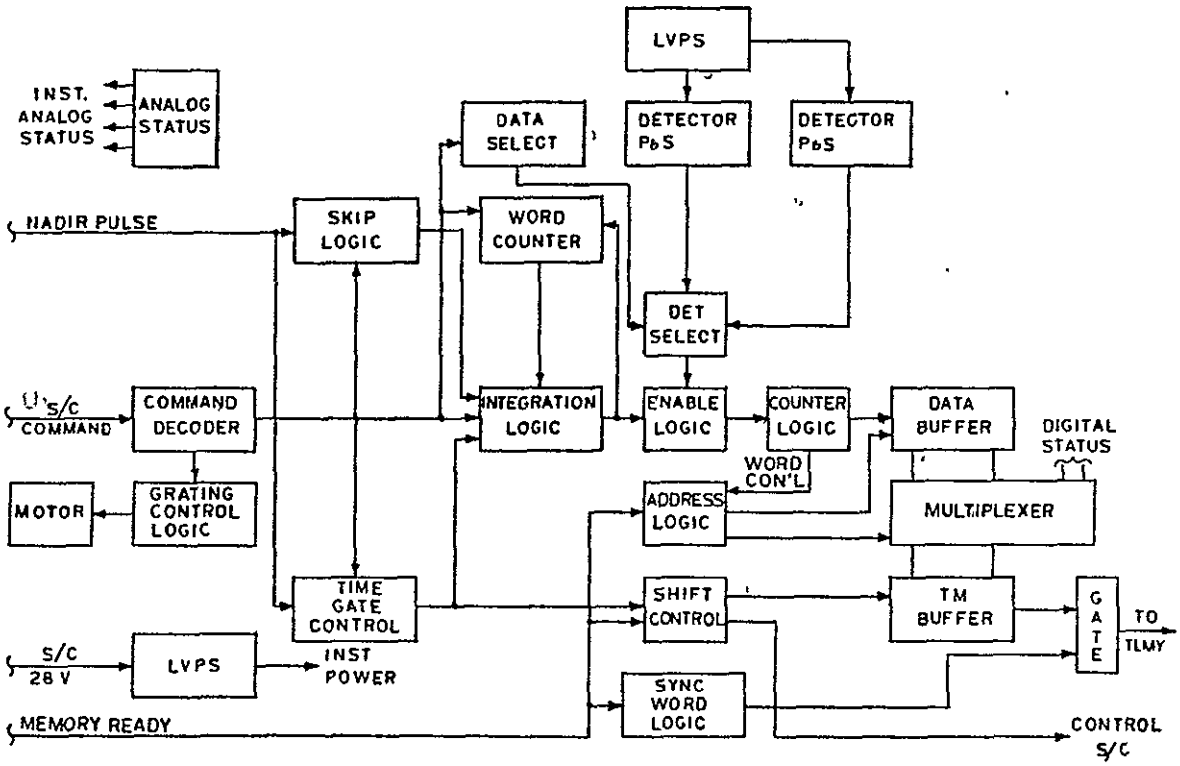

1.27μ AIRGLOW INSTRUMENT BLOCK DIAGRAM

Figure 3.13

3.3.6 Instrument Physical Characteristics

Weight	6.0 lbs
Size	14" x 6" x 4½"
Power	1.5 watts
Telemetry	20 data words per spacecraft rotation
Duty Cycle	from 0.40 sec to 1.60 sec per spacecraft rotation
Command	two command words
Pointing Requirement	spin axis must be parallel to the limb to $\pm 3°$
Temperature	20 °C $\pm$ 40 °C

3.4 Visible Nitrogen Dioxide Experiment

3.4.1 General

The determination of nitrogen dioxide concentrations in the 20-40 km region of the atmosphere will be made by observing the NO_2 absorption of Rayleigh scattered sunlight at the limb. The instrument proposed to make these measurements is a programmable Ebert-Fastie spectrometer of the same basic design used for the ultraviolet ozone experiment, the 1.27μ airglow instrument, and the solar ultraviolet monitor. The basic instrument is described in Section 3.1 and is shown in Figure 3.14. All optical coatings will be maximized for the visible. The grating will have a ruling density of 1200 lines/mm blazed at 8800 A. The dispersion at the exit slit is about 24 A/mm at 4400 A in second order. Two closely spaced exit slits will be used to observe the

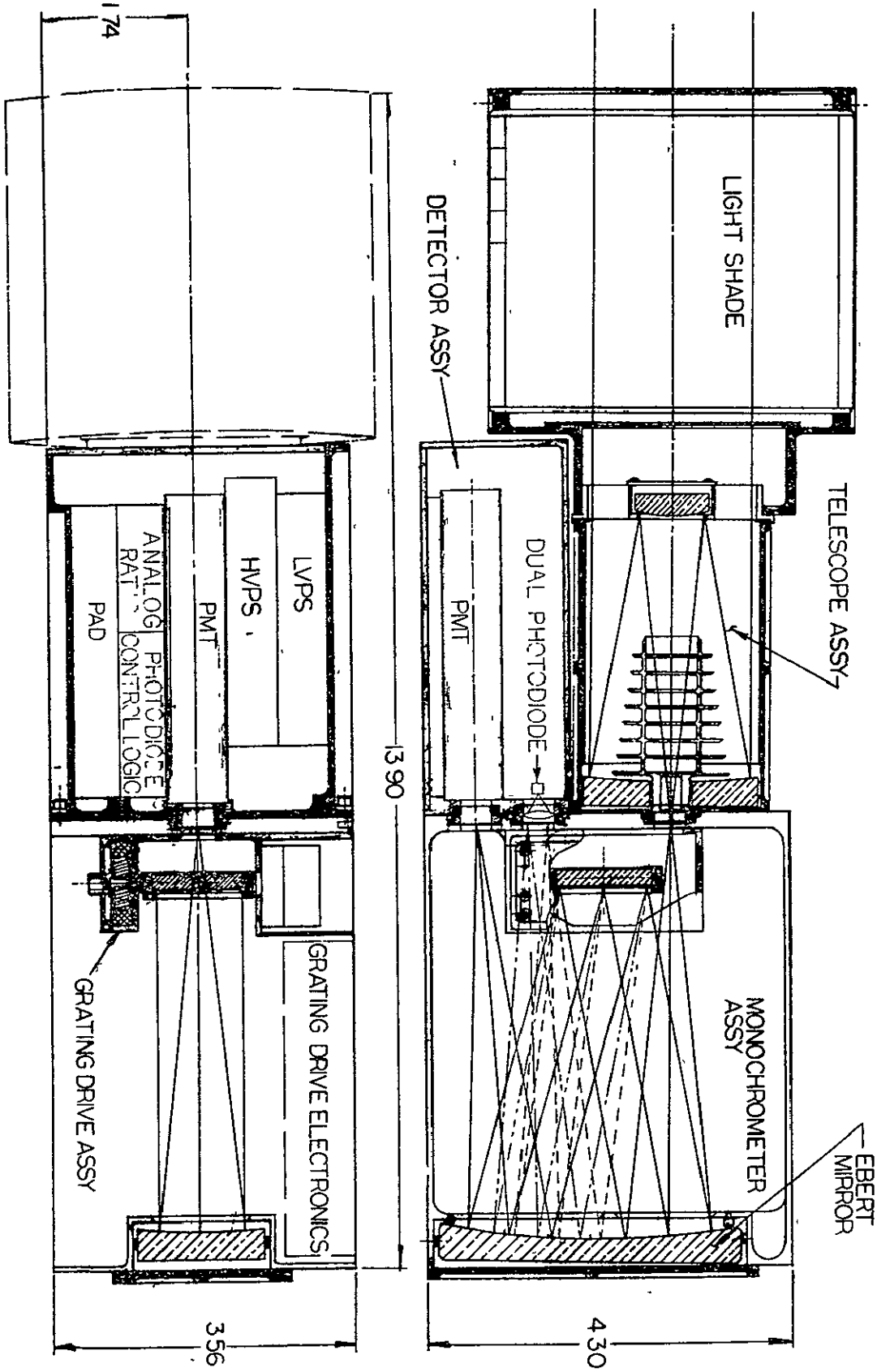

Figure 3.14 Visible Nitrogen Dioxide spectrometer

differential absorption of NO_2 near 4400 A in second order. Entrance and exit slits will all be 0.44 mm wide giving an altitude resolution of 3.5 km and a spectral resolution of 10.6 A. The exit slit separation will be 3.5 mm in order to have one slit at 4390 A where NO_2 absorption is maximum and the other at 4480 A where absorption is minimum.

3.4.2 Detectors and Sensitivity

The two exit slits will be imaged on a dual silicon photodiode. The output of these diodes will be amplified and their ratio taken and digitized. Because of the high signal level and small absorption photodiodes will be used rather than photomultipliers.

The photon flux arriving at the detector's ranges from 10^9 sec^{-1} to 2 x 10^{10} sec^{-1} as the point of closest approach to the earth's surface decreases from 40 km to 20 km. At such high flux rate ordinary photomultiplier tubes saturate. Rather than attenuate the high signal we have chosen to use photodiode detectors whose equivalent noise (for a 3 ms integration time) is 5 x 10^6 photons/sec. The resulting signal to noise thus ranges from 300 to 4000 over the 20-40 km height interval thus permitting an absorption of 0.3% or less to be measured. Except at high winter latitude this will allow extraction of the NO_2 profile with 3.5 km height resolution and 10% uncertainty in density over the altitude range where NO_2 is important. At high winter latitude, where the maximum limb absorption will be

approximately 0.5%, we can still locate the altitude of maximum density and determine the density to 20% uncertainty using an average of several limb scans.

A third exit slit with an E-type photomultiplier (tri-alkali photocathode) will be used to measure atmospheric radiation at high altitudes and to determine the wavelength calibration.

3.4.3. Data and Telemetry

The basic operating procedure is similar to that used in the ultraviolet ozone experiment except that the height interval will be limited to the 15-50 km range, with occasional spectral scans of the earth's surface below.

3.4.4 Commands and Modes of Operation

Figure 3.15 is a block diagram for the nitrogen dioxide experiment. In the standard mode used for limb scans, the grating will be programmed to align the two exit slits at 4390 and 4480 A. Once each satellite rotation, when the instrument views in the nadir direction the two outputs will be normalized; the NO_2 absorption looking down will usually not exceed 0.15%. Whatever the actual stratospheric absorption the downward absorption will be 40 times less except near large cities. Any tropospheric pollution sources could be easily recognized and removed. The change in the signal ratio as the limb is scanned then gives the information on nitrogen dioxide. By altering the slit pair to other wavelengths, it will be possible to check the nitrogen dioxide

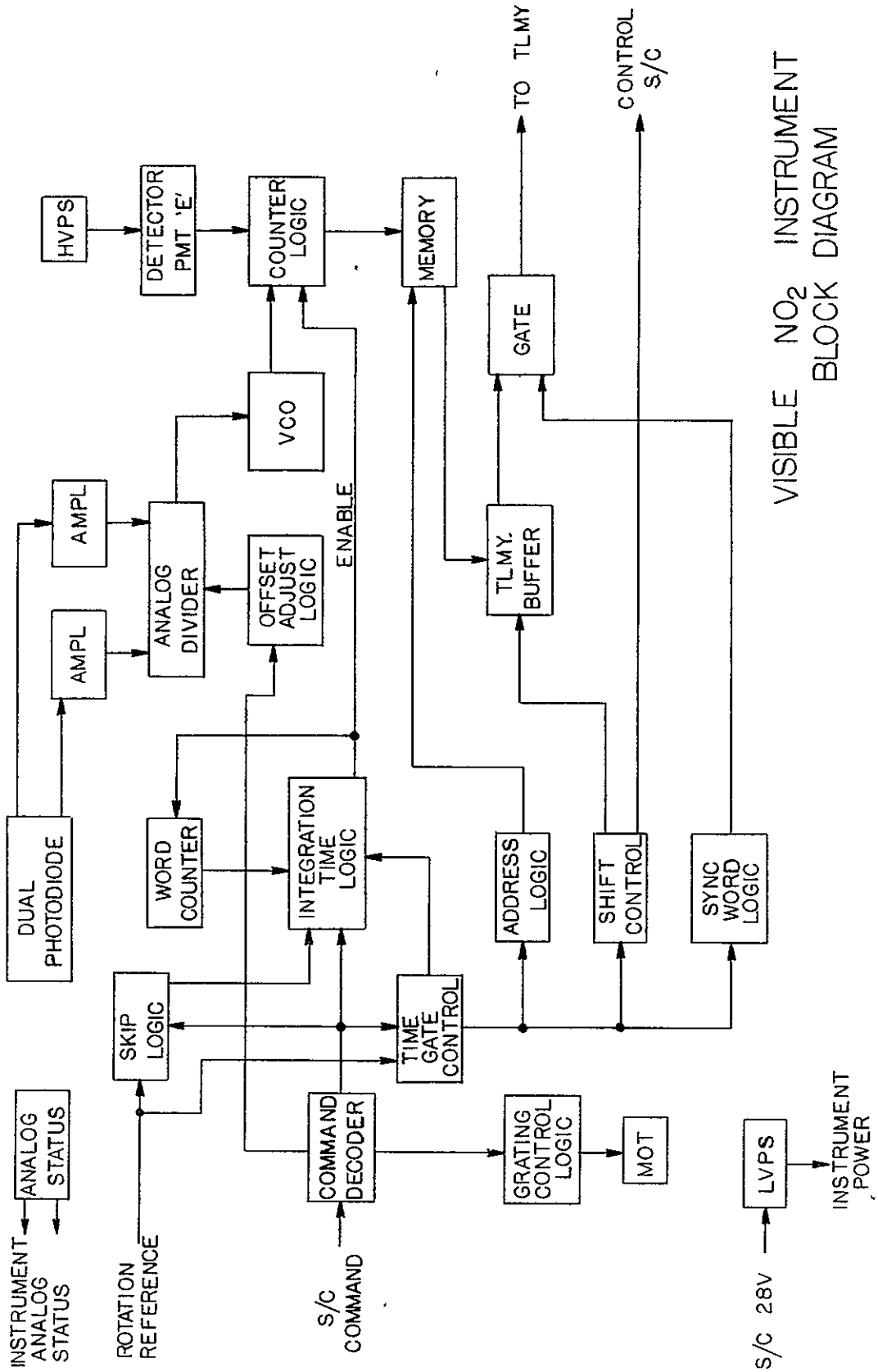

Figure 3.15

measurements; for example a pair of wavelengths at which the NO_2 absorption coefficient is the same should show no variation in their ratio as the limb is scanned.

In the normal mode all limb scans will be taken at 3 ms gate time; however, we use two command bits to permit 1, 2, 4, 8, ms gate times. Fourteen command bits will be required to specify the time of data start. One bit describes whether the mode is scanning or fixed wavelength and six bits specify the grating position.

3.4.5 Instrument Physical Characteristics

Weight	Spectrometer	3.5 lbs
	Logic	2.0 lbs
	Telescope	0.5 lbs
	Total	6.0 lbs
Size	Spectrometer, 10½" x 5½" x 4½"	
	Spectrometer and Telescope, 14" x 6" x 4½"	
Power	1.5 watt	
Telemetry	40 data words per spacecraft rotation	
Duty Cycle	from 0.40 sec to 1.60 sec per spacecraft rotation	
Command	two command words	
Pointing Requirements	Spin axis must be parallel to the limb to $\pm 3°$	

3.5 Solar Ultraviolet Monitor

3.5.1 General

The proposed instrument is a 1/8 meter Ebert-Fastie spectrometer. The instrument is of the same basic design as the spectrometer described in Section 3.1 and will monitor the solar flux scattered from a diffusing screen. The spectrometer will operate in two modes: (1) it will scan the spectral range 1600 A to 3100 A by rotation of the grating; (2) the grating will be set to a desired wavelength, and the instrument will continually monitor the solar flux at that wavelength and at another wavelength 600 A away. The bandpass of the spectrometer will be fixed at 20 A for both wavelength channels.

3.5.2 Instrument Configuration

The basic layout of the ultraviolet solar instrument is shown in Figure 3.16. The instrument will be mounted in the side of the spacecraft and will scan through the sun once per spacecraft revolution. Solar radiation will enter through a hole in the spacecraft skin (0.2" x 3" cylindrical section) onto the diffusing screen which will scatter the solar radiation into the spectrometer.

3.5.3 Optical Layout

The diffusing surface will be a thin layer of MgF_2 and will scatter the incident solar radiation isotropically.

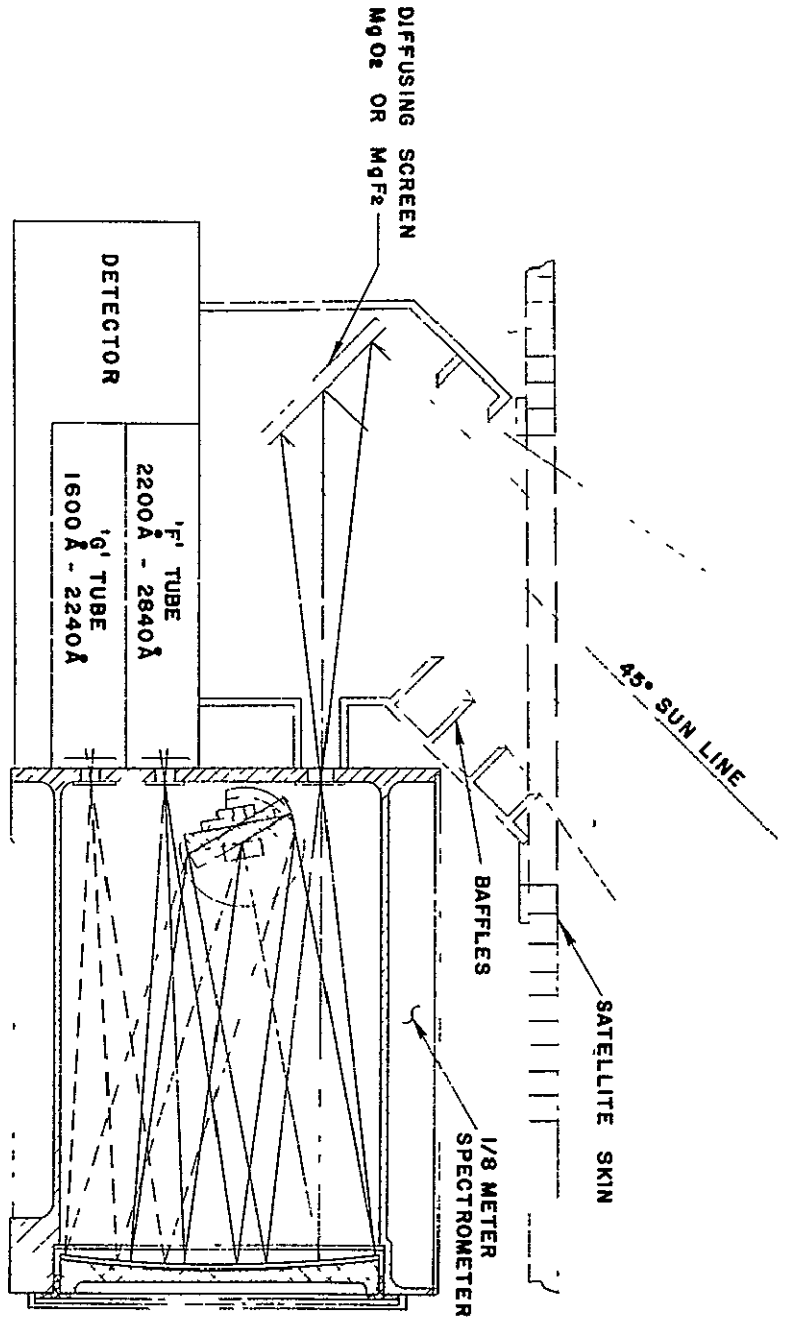

SOLAR INSTRUMENT

Figure 3.16

The screen design allows the angle of incident solar radiation to vary $\pm 10°$ with a minimum change in the scattered intensity.

The f/5 spectrometer will have a spherical Ebert mirror with 12.5 cm focal length. The grating will have 2400 lines/mm and will be blazed at 1500 A. All of the spectrometer optics will be coated with Al and MgF_2. The spectrometer entrance slit will be 0.64 mm wide by 15 mm long ($A_s = 1.0 \times 10^{-2}$ cm^2). The spectrometer will have two exit slits separated by 2 cm (600 A): (1) a 0.67 mm x 2.0 mm exit slit for the G channel, and (2) a 0.034 mm x 2.0 mm exit slit for the F channel. The spectrometer bandpass of 20 A will be determined by the width of the entrance slit.

3.5.4 Diffusing Screen

The diffusing screen will be a 3" glass or aluminum plate. The diffusing surface will probably consist of a glass bead surface, although other surfaces, for example MgF_2 or $BaSO_4$, will be evaluated in terms of their scattering efficiency at short and long wavelengths and their overall stability. Various surfaces will be evaluated to determine their relative scattering coefficients and their ability to approximate a true Lambert surface.

3.5.5 Detector

There are two detectors with separate pulse counting electronics. The short wavelength detector will be a 510 G phototube (CsI photocathode) with a MgF_2 window and will

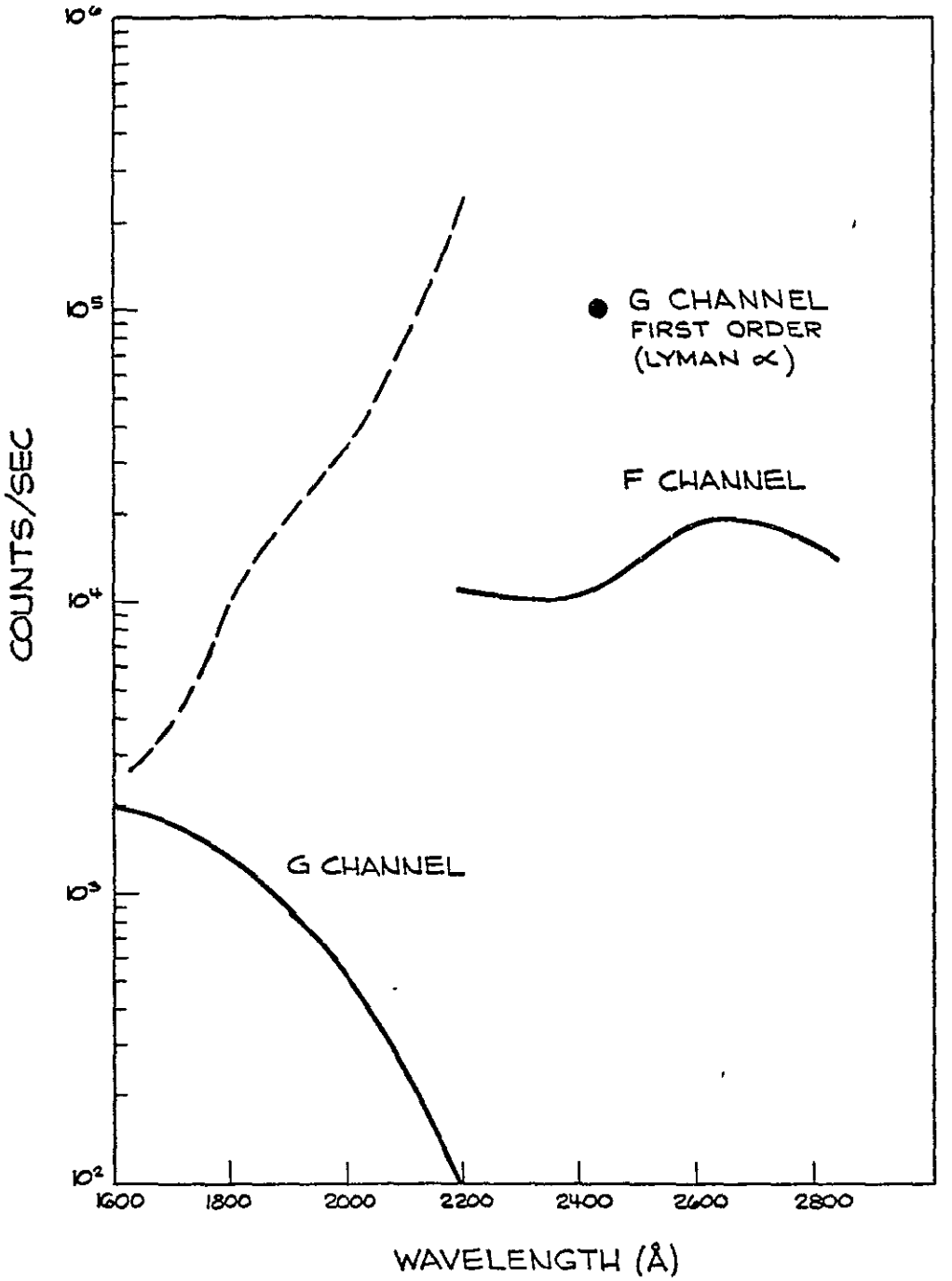

SOLAR INSTRUMENT RESPONSE CURVES

Figure 3.17

measure solar radiation in the spectral region 1600 A to 2500 A, and 1150 A to 1250 A. The long wavelength detector will be a 510 F phototube (CsTe photocathode) with a quartz window and will be used in the spectral region 2200 A to 3100 A.

The pulses from the photomultiplier tubes will be fed through a PAD circuit, and the output pulses are about 100 ηsec long by 10 volts high. Dead time of this circuit is on the order of 50 ηsec, and the circuit will saturate only for count rates greater than 7 MHz.

The pulse counters will have programmable gate times of 16 msec, 32 msec, 64 msec, and 128 msec. Figure 3.17 is a plot of the expected count rates for each of the two channels, and it is clear that the total counts accumulated will vary from a few counts per gate time to approximately 3000 counts per gate time. The dashed portion of the curve at short wavelengths shows the response of the short wavelength channel using an F tube in place of the G tube. The use of such a detector will be desirable if instrument scattered light is down four orders of magnitude.

3.5.6 Data Storage and Telemetry

Figure 3.18 is a schematic block diagram of the ultraviolet solar experiment electronics. Since the timing of the solar experiment is not keyed to the limb sensor, a solar sensor initiates the data stream. This sensor will be boresighted such that it sends a solar presence pulse when

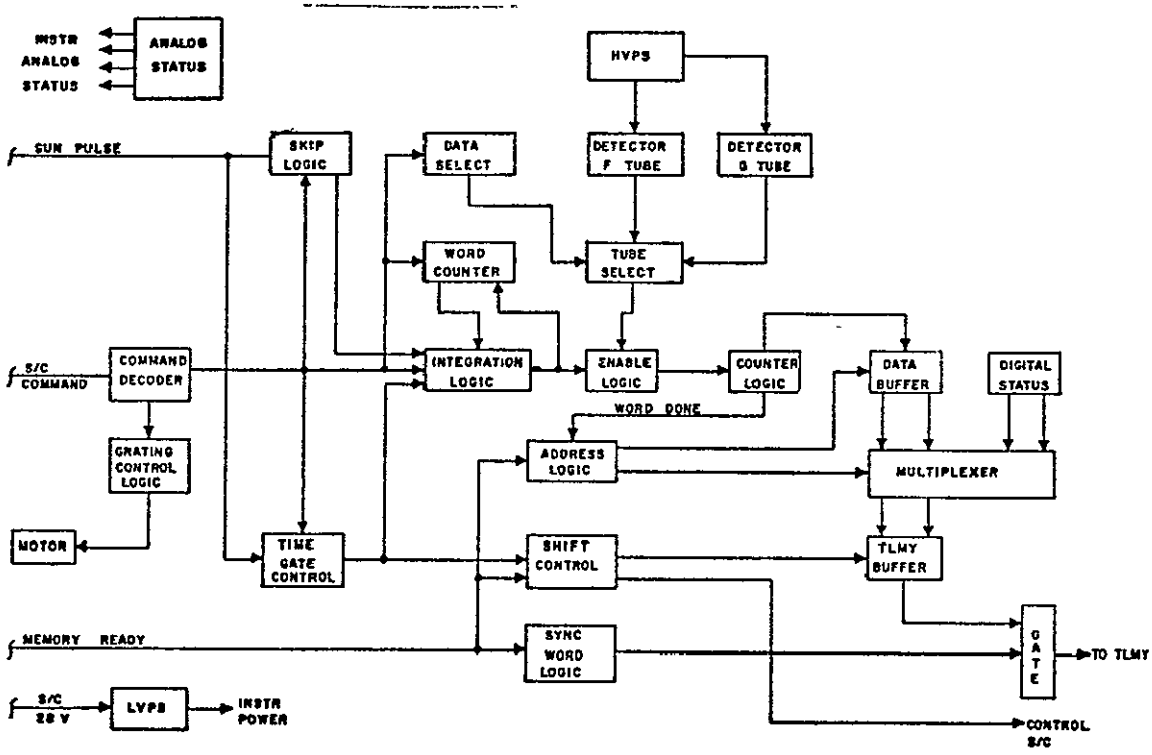

Figure 3.18 Ultraviolet Solar Experiment Electronics Block Diagram

the scattered sunlight first fully illuminates the spectrometer field of view. Upon receipt of this pulse the pulse counter will wait for W gate times (see command below) and then shift its contents to a storage register at each of ten subsequent gate times. During this data accumulation time, the satellite will rotate from 4.8° to 40° depending on the specified gate time. The satellite telemetry system may then request up to N data words from the storage register once per spacecraft revolution.

3.5.7 Commands and Modes of Operation

The mode of operation of solar experiment will be specified by the following commands. One bit will specify choice of phototube, and two bits will select one of the four gate times. There are two data taking registers to be specified. One specifies the number, W, of data words to skip following a solar presence signal before shifting counts into the storage register. The second, N, specifies the number of data words to be taken from the storage register and telemetered each revolution. Finally, there are two basic modes of spectrometer operation, a scanning mode and a fixed mode. There are 64 positions of the grating drive (64 steps where each step corresponds to a 14 A shift in wavelength). In the scanning mode, the drive is initiated to the lower wavelength limit and is stepped once per spacecraft rotation, thus completing a full spectral scan (for one channel only) every 12.8 minutes, or once per

orbit. In the fixed mode, a wavelength position is specified (6 bits), and the drive slews to that position and remains there until another mode command is received. This mode is used to monitor the solar flux at a given wavelength for many spacecraft revolutions.

3.5.8 Instrument Physical Characteristics

Weight	Spectrometer	3.5 lbs
	Logic	2.0 lbs
	Diffusion Cell	0.5 lbs
	Entrance Baffle	0.5 lbs
	Total	6.5 lbs

Size — Spectrometer and Diffusing Cell, 14" x 6" x 4½"

Power — 7.8 watts

Telemetry — Up to eight data words per spacecraft rotation. Normal mode would be one word per revolution

Duty Cycle — from 0.16 sec to 1.28 sec for each spacecraft rotation (12.0 sec)

Command — two command words completely specify instrument operation

Pointing Requirements — ±10° for spin axis

4.0 EXPECTED RESULTS

The primary anticipated result is the determination of the nature and magnitude of changes in mesospheric ozone densities that are the result of changes in the solar ultraviolet flux. As part of this result, we expect to determine whether variations in the Schumann-Runge region, 1750-2100 A, in the Hartley region, 2000-3000 A, or at Lyman alpha, 1216 A, cause changes in the ozone content of the 50-70 km altitude region. It is first necessary to determine whether an increase in the solar flux in the Schumann-Runge region leads to an increase or a decrease in the ozone density. The uncertainty arises because this part of the solar flux dissociates both molecular oxygen to form atomic oxygen and water vapor to form atomic hydrogen, hydroxyl, and perhydroxyl. Atomic oxygen forms ozone, and the products of water vapor dissociation destroy ozone. The magnitude of the changes in ozone density will also be determined.

A second result will be an understanding of the relationship between solar flux, ozone, and the temperature of the mesosphere. A change in temperature may lead to a change in the ozone density through the temperature sensitivity of the relevant reaction rates. Conversely, a change in the ozone density will produce a change in the temperature since ozone heats the mesosphere through the conversion

of solar photon energy to the kinetic energy of its dissociation products. Finally, changes in the solar flux may change the mesospheric temperature, either through its interaction with ozone or by other, less direct mechanisms. Correlation of the observed variations in the flux, ozone density, and temperature will determine the sign and magnitudes of these interrelated dependences.

A third anticipated result is an understanding of the relationship between ozone and water vapor. An increase in the abundance of water vapor in the mesosphere should lead to a decrease in the amount of ozone because the dissociation products of water vapor destroy ozone. However, the effect is complex, involving the degree of screening of water by molecular oxygen, the density and temperature dependent rates of the reaction cycles which consume the ozone, and the rate at which the catalysts (atomic hydrogen, hydroxyl, and perhydroxyl) are converted to stable forms such as molecular hydrogen. The solar flux enters the picture through the photodissociation process, and the temperature enters through reaction rates. Once more the systematic observations of changes in the fundamental quantities will establish the nature of the relationships and illuminate their details.

It is anticipated that having established the direct relationships between ozone and the solar flux, water vapor, and temperature, we will be able to determine if there are

changes in mesospheric ozone arising from other causes. An example is the occurrence of solar proton events. If a sufficient number of events occurs during 1979-80, the following results are anticipated: the relationship between the magnitude of decrease in ozone and the flux and energy of the solar protons, the recovery rate of the ozone following the event, and the role of water vapor in the solar proton destruction of ozone.

Finally, we anticipate that with our increased and more precise understanding of the interrelationships of ozone, solar flux, water vapor, and temperature in the mesosphere, we will better understand the stability of ozone against changes of any kind in mesospheric conditions. We also anticipate that this increase in understanding will usefully extend into the stratosphere, where the bulk of the earth's ozone exists, and where the questions of ozone fluctuations and stability are of importance to the environment at the surface of the earth.